International Communications in Heat and Mass Transfer 87 (2017) 132–146

Contents lists available at ScienceDirect

International Communications in Heat and Mass Transfer

journal homepage: www.elsevier.com/locate/ichmt

Improved social spider optimization algorithms for solving inverse radiation and coupled radiation–conduction heat transfer problems

Shuang-Cheng Sun, Hong Qi*, Ya-Tao Ren, Xiao-Ying Yu, Li-Ming Ruan*

School of Energy Science and Engineering, Harbin Institute of Technology, Harbin, Heilongjiang 150001, PR China

A R T I C L E I N F O

Keywords:
Improved SSO algorithm
Parameter estimation
Coupled radiation-conduction
Inverse radiative heat transfer

A B S T R A C T

A novel bio-inspired swarm algorithm, social spider optimization (SSO), is introduced to solve the inverse transient radiation and coupled radiation–conduction problems for the first time. Based on the original model, five improved SSO (ISSO) algorithms are developed to enhance search ability and convergence velocity. The sensitivity analysis of measured signals with respect to the physical parameters of the medium are described. After which, the SSO and ISSO algorithms are applied to solve the inverse estimation problems in a one-dimensional participating medium. Two cases concerns radiative transfer problems are investigated, in which the radiative source term, extinction coefficient, scattering albedo, and scattering symmetry factor are reconstructed. Furthermore, the coupled radiation–conduction heat transfer model is considered and the main parameters such as the conduction–radiation parameter, boundary emissivity, and scattering albedo are retrieved. All retrieval results show that SSO-based algorithms are robust and effective in solving inverse estimation problems even with measurement errors. Findings also show that the proposed ISSO algorithms are superior to the original SSO model in terms of computational accuracy and convergence velocity.

1. Introduction

Radiation and coupled radiation–conduction heat transfer exist in various industrial fields. Inverse heat transfer problems have been widely studied in numerous research fields, such as the combustion diagnosis in high-temperature flame, reconstruction of the temperature distribution and the optical parameters in combustion chambers, remote sensing in atmospheric science, optical tomography in medical imaging, and inverse design of radiative enclosures [1–6]. Meanwhile, a great quantity of inverse techniques have been proposed and developed to solve the problems of inverse heat transfer. Most of these techniques are accomplished by optimizing a certain objective function. The extinction coefficient, scattering albedo, boundary emissivity, scattering phase function, conduction–radiation parameter, particle size, and the pre-desired heat flux distribution on the specified boundary are successfully retrieved [7–36].

The theoretical techniques for solving inverse heat transfer problems can be generally classified into two groups: the gradient-based method (or deterministic algorithm) and the random search-based method (or stochastic/evolutionary-based optimization algorithm). Numerous estimation problems have been solved by the gradient-based method due to its high computational efficiency. For example, the conjugate gradient method (CGM) was employed to solve the inverse radiation heat transfer problems for retrieving the radiative properties and temperature distribution of media by Li et al. [8] and Salinas [11]. Howell et al. [17] and Bayat et al. [19] applied CGM to the inverse design of radiative enclosures, and Daun et al. [18] compared the advantages and disadvantages between CGM and other regularization methods for solving inverse design problems. The retrieval results showed that the CGM needed less CPU time with less storage requirements. Neto et al. [14] and Ren et al. [15] studied the inverse estimation of radiative properties and temperature distribution of media through the Levenberg–Marquardt (L–M) method, respectively. Good agreements between measured and estimated measurement signals were obtained. The CGM and L–M methodhad also been extensively investigated for solving the parameter identification [20,21] and inverse design problems [22,23] involving coupled radiation–conduction heat transfer. Lots of studies demonstrated that the gradient-based method was robust and efficient in solving inverse heat transfer problems.

However, the process for retrieving the gradient in the above gradient-based optimization techniques is quite difficult. Also, the retrieval results strongly depend on the initially guessed values, and even an unfeasible solution can be obtained if the initial value is unsuitable. In the recent decades, many swarm intelligence algorithms, including differential evolution (DE) [24,25], genetic algorithm (GA) [26,27],

* Corresponding author at: School of Energy Science and Engineering, Harbin Institute of Technology, 92, West Dazhi Street, Harbin 150001, PR China.
E-mail addresses: qihong@hit.edu.cn (H. Qi), ruanlm@hit.edu.cn (L.-M. Ruan).

http://dx.doi.org/10.1016/j.icheatmasstransfer.2017.07.010

Available online 04 August 2017
0735-1933/

Nomenclature

a	coefficient in radiative source term
c	speed of light
c_p	specific heat capacity at constant pressure
c_v	specific heat capacity at constant volume
ct_p	pulse laser width
d	Euclidian distance
g	scattering asymmetry factor
$\mathbf{F}$	a vector consists of female spiders' positions
F_{obj}	objective function
h	convective heat transfer coefficient
I	radiative intensity
J	fitness value
L	thickness of media
LB	lower bound
$\mathbf{M}$	a vector consists of male spiders' positions
n	refractive index
$\mathbf{n}$	normal vector
N	the total number of spider population
N_{cr}	conduction-radiation parameter
N_f	the number of female spiders
N_m	the number of male spiders
NN	the number of involved mating spiders
N_n	the number of measured signals
PF	a threshold
PM	mutation probability
$rand$	a uniform distribution random number
R	reflectance
$\mathbf{s}$	scattering direction
$\mathbf{s}'$	incident direction
S	radiative source term
q	power density
q_r	radiative heat flux
t	iteration number or time
T	temperature
UB	upper bound
Vib	vibration
w	weight
x	position in the medium
$\mathbf{X}$	a vector consists of spiders' positions

Greeks symbols

α	a uniform distribution random number
β	a uniform distribution random number
β_e	extinction coefficient
χ	acceleration coefficient
δ	a uniform distribution random number
$\boldsymbol{\delta}$	Dirac's delta function
Δ	a fluctuation
ΔS	search step
Δt	time step
ε	computational accuracy or boundary emissivity
ε_{rel}	relative error
γ	a uniform distribution random number or measurement error
ϕ	a uniform distribution random number
Φ	scattering phase function
η	amplification coefficient
φ	a uniform distribution random number
ϑ	excess temperature
κ_a	absorption coefficient
κ_s	scattering coefficient
λ	thermal conductivity
μ	directional cosine
Θ	dimensionless temperature
ρ	density
σ	standard deviation or Stefan-Boltzmann constant
τ	optical thickness
ω	inertia weight or scattering albedo
Ψ	sensitivity coefficient
ς	a normal distribution random value

Subscripts

b	blackbody or the best spider
best	the best value
c	collimated value or the closest neighbor spider
cal	calculated value
exa	exact value
d	scattered light
est	estimated value
f	female spider
i	ith spider
h	historical value
in	incident value
j	jth spider
L	the right boundary
m	male spider
max	the maximum value
mea	measured value
min	the minimum value
s	ambient value
w	boundary
worst	the worst value

particle swarm optimization (PSO) [28–30], ant colony optimization (ACO) [31–33], krill herd (KH) [34,35], have been proposed and applied in various industrial fields. These algorithms can effectively overcome the drawbacks and limitations of the above conventional gradient-based techniques. Moreover, the intelligent algorithms can deal with lots of feasible solutions at each iteration and all the processes are performed in parallel. These algorithms are significantly superior to the gradient-based method in terms of achieving global optimal values and computational stability, especially for higher dimensional problems [36,37]. Li et al. [26] applied GA to estimate the single scattering albedo, optical thickness and phase function in an azimuthally symmetric, absorbing, anisotropically scattering parallel slab simultaneously. All the parameters were accurately reconstructed. The authors pointed out that the inverse radiation problem considered in this study was difficult to be solved by traditional optimization methods, whereas GA was quite robust in solving this optimization task even with measurement errors, demonstrating the superiority of the intelligent algorithm. Bokar [38] studied the simultaneous estimation of the optical thickness and the spatially varying albedo in a one-dimensional (1D) parallel slab filled with inhomogeneous gray medium. The direct problem was solved by the discrete ordinate method (DOM), and the artificial neural networks (ANN) algorithm was utilized to estimate the determined optical thickness and the varying scattering albedo that was expressed in a polynomial form. The retrieval results showed that accurate estimation results could only be obtained in small optical thickness through the ANN algorithm. Qi et al. [30] firstly introduced the PSO algorithm in solving the inverse radiation problems and applied the stochastic PSO (SPSO) algorithm to estimate the source term, extinction coefficient, scattering coefficient, and non-uniform absorption coefficients in a 1D radiating gray plane with gray boundaries. All the above radiation parameters were accurately estimated even with noisy data, which provided a new robust tool for solving inverse radiation problems.

Meanwhile, the intelligent algorithms had also been extended and applied to various inverse coupled radiation–conduction heat transfer problems. Das et al. [27] investigated the simultaneous estimation of the emissivity, temperature distribution, and heat flux on the left boundary in a 1D transient radiation–conduction heat transfer problem through the GA. The effects of the measurement errors and control parameters in the GA such as the population size and the iteration number on the estimation results were also discussed. Chopade et al. [25] simultaneously estimated the extinction coefficient, scattering albedo, emissivity, and conduction–radiation parameter in the participating medium with diffused gray boundaries using the DE algorithm. The DE algorithm achieved superior performance compared with GA in terms of computational accuracy. Qi et al. [39] proposed a hybrid KSM–PSO algorithm, in which the K-means clustering and the simplex method were combined with the standard PSO. The conduction–radiation parameter, scattering albedo and boundary emissivity in 1D semi-transparent medium were simultaneously estimated using PSO algorithms, and the proposed KSM–PSO was proved to be more efficient and accurate than PSO and simplex bare-bones PSO algorithms. However, most of the above intelligent algorithms have the common drawbacks of time–consuming calculation and slow convergence velocity, especially during the final iterations.

A novel bio-inspired optimization technique, called social spider optimization (SSO) algorithm, was proposed in 2013 by Cuevas et al. [40]. In the SSO algorithm, the spiders are divided into two groups according to their gender, and the individuals emulate interaction with one another based on the biological laws of a cooperative colony through a communal web. Each spider is conducted by a set of different evolutionary operators, which mimic different cooperative behaviors that are typically found in the colony. Female spiders tend to present an attraction or dislike toward others. The attraction or dislike is commonly encoded as small vibrations that are critical for the collective coordination of all individuals. The vibrations for a particular spider are determined by the weight of other spiders and the distance between two individuals. Thus, a strong vibration is produced by a spider with good fitness or the neighbor spider of the specified one. Male spiders are divided into dominant and non-dominant populations according to their weights. The dominant male spiders are attracted to the closest female spider, whereas the non-dominant male spiders tend to concentrate upon the center of the male population [40–42]. In addition, mating, which is performed by dominant male spiders and their neighbor female spiders, is an important operation in SSO. Mating operation is assigned by the roulette method, which allows the individuals to exchange information and increase population diversity [40]. A comprehensive set of 19 functions were tested to examine the performance of the SSO algorithm. All the retrieval results showed that SSO algorithm achieved higher accuracy than those obtained by both PSO and artificial bee colony (ABC) algorithms [40]. Cuevas et al. [43] proposed a novel swarm algorithm, called SSO-C, based on the original SSO to solve constrained optimization tasks. For these problems, a penalty function introduces a tendency term into the original objective function to penalize the constraint violations, thereby solving a constrained task as an unconstrained one. A feasibility criterion was applied to bias the new individuals toward feasible regions. Eight well-defined constrained benchmark functions were tested to assess the performance of SSO-C algorithm, and the retrieval results were compared with those obtained by PSO, ABC and firefly method, which demonstrated the superiority of the SSO-C algorithm. To date, SSO algorithms have been successfully applied to the detection of energy theft [44] and the training of artificial neural networks [45,46].

However, to the best knowledge of the authors, reports have not yet been conducted about the application of SSO algorithm for solving problems of inverse estimation tasks in radiation or coupled radiation–conduction heat transfer. Thus, this study aims to introduce the SSO algorithm to solve the inverse transient radiation and coupled radiation–conduction problems in an absorbing, scattering, and emitting parallel slab with diffuse and gray boundaries. Five improved SSO (ISSO) algorithms are proposed to accelerate convergence efficiency and search ability, thereby improving the computational performance of the original SSO algorithm. Furthermore, both the original SSO and ISSO algorithms are applied to estimate the multi-parameters in transient radiation and coupled radiation–conduction problems simultaneously.

The remainder of this work is organized as follows. In Section 2, the theoretical overview of the SSO algorithm is introduced thoroughly, and five ISSO algorithms are proposed to improve the search ability of the spider population and accelerate the convergence velocity. Section 3 describes the TRTE in radiation problems and the additional energy equation in conduction problems. The inverse estimation results are also presented in this section. First, the distribution of the radiative source term in radiation problems is estimated by SSO algorithms, and the comparison between SSO and ISSO algorithms is discussed. Afterwards, the sensitivities of the reflectance with respect to the extinction coefficient, scattering albedo, and scattering asymmetry factor in radiation problems are analyzed. Subsequently, these three parameters are simultaneously reconstructed. Finally, the sensitivities of the dimensionless temperature on the boundaries with respect to the conduction–radiation parameter, scattering albedo, and boundary emissivity in coupled radiation–conduction problems are analyzed. Thereafter, these three parameters are simultaneously estimated. The main conclusions and perspectives are presented in Section 4.

2. Inverse model

2.1. SSO algorithm

SSO algorithm is a novel bio-inspired swarm algorithm for solving optimization problems based on the cooperative behavior of social spiders [40]. In SSO algorithm, the spider population is divided into two search groups according to their genders (female and male), and their positions are updated at each iteration according to different evolutionary operators. Meanwhile, the communal web allows the spiders to communicate with each one another to transmit important information, which accelerates finding the optimal position for the spider population. A schematic of the movement of spiders is presented in Fig. 1.

Social spiders are highly female-based population, and the number of male spiders hardly reaches 30% of the entire population. In SSO algorithm, the number of females is randomly determined in the range of 65%–90% of the whole spider swarm, which can be expressed as [40]:

$$N_\mathrm{f} = \mathrm{floor}[(0.9 - rand \times 0.25) \times N] \tag{1}$$

where floor(·) is the function that maps a real number to an integer number, N_f and N represent the numbers of female and total spiders, respectively, and *rand* is a random number in the interval of [0, 1]. Therefore, the number of male spiders can be calculated as follows:

$$N_\mathrm{m} = N - N_\mathrm{f} \tag{2}$$

where N_m is the number of male spiders.

In the social spider swarm, the size of each spider is different, and all the spiders have their own role for accomplishing their assigned tasks. Weight is introduced to emulate the size of spiders, which is calculated by individual fitness [40]:

$$w_i = \frac{J_i - J_\mathrm{worst}}{J_\mathrm{best} - J_\mathrm{worst}} \tag{3}$$

where J_i indicates the fitness of the *i*th spider. J_worst and J_best represent the worst and best fitness of the entire spider population so far, respectively.

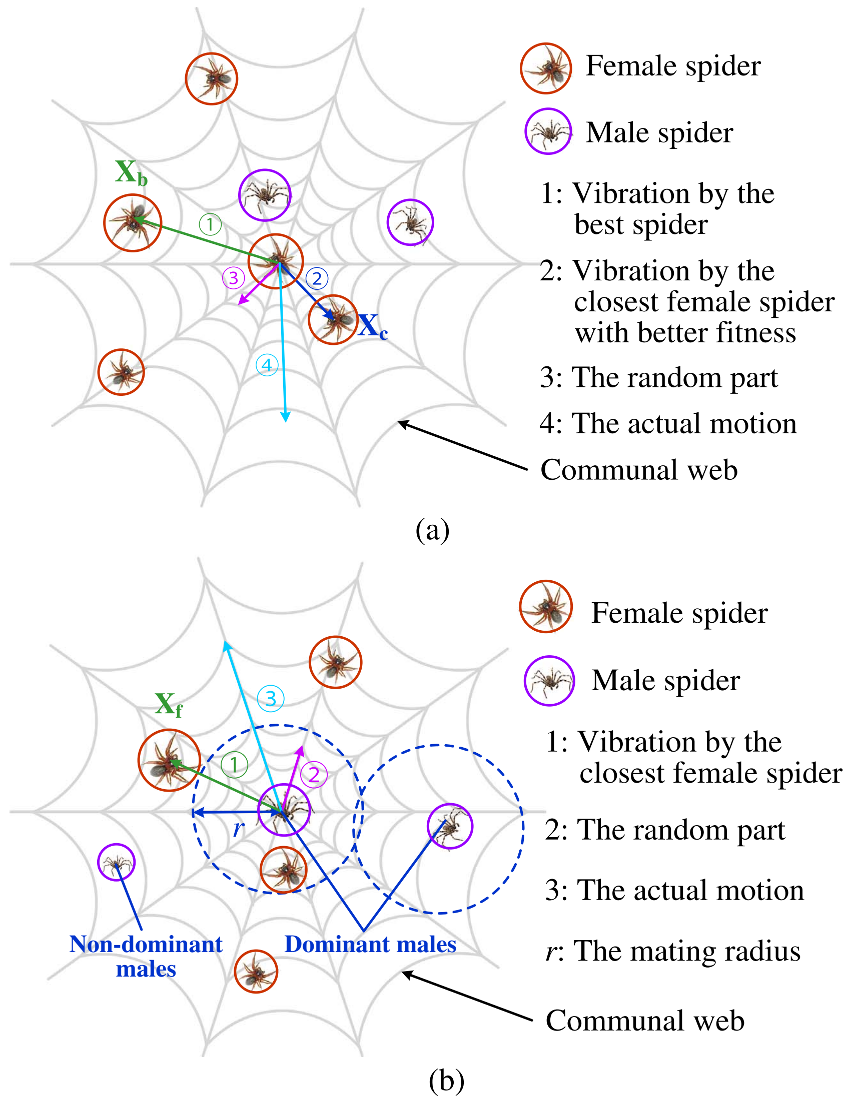

Fig. 1. The schematic of the movement of (a) female and (b) male spiders.

Individual spiders exchange information through the communal web, and this communication among spiders is emulated by small vibrations, which can be formulated as [40]:

$$Vib_{i,j} = w_j \cdot \exp(-d_{i,j}^2) \tag{4}$$

where $d_{i,\ j}$ denotes the Euclidian distance between the ith and jth spiders, and $d_{i,j} = \|X_i - X_j\|$.

The female spiders may perform attraction or repulsion over other spiders, which can be modeled as [40]:

$$\mathbf{F}_i^{k+1} = \begin{cases} \mathbf{F}_i^k + \alpha \cdot Vib_{c_i} \cdot (\mathbf{X}_c - \mathbf{F}_i^k) + \beta \cdot Vib_{b_i} \cdot (\mathbf{X}_b - \mathbf{F}_i^k) + \phi \cdot (rand - 0.5) & \delta \leq PF \\ \mathbf{F}_i^k - \alpha \cdot Vib_{c_i} \cdot (\mathbf{X}_c - \mathbf{F}_i^k) - \beta \cdot Vib_{b_i} \cdot (\mathbf{X}_b - \mathbf{F}_i^k) + \phi \cdot (rand - 0.5) & \text{else} \end{cases} \tag{5}$$

where α, β, ϕ, $rand$, and δ are random numbers in the interval of [0, 1]. $\mathbf{X}_c$ and $\mathbf{X}_b$ represent the positions of the closest spider to the ith spider that holds a higher weight and the best spider of the entire population, respectively. PF denotes a threshold that can control the movement toward attraction or repulsion.

The male spiders are divided into two different groups, dominant and non-dominant, based on their weight, and they are distinguished by the median spider. The dominant spiders are the individuals who are heavier than the median member and are attracted to the closest female member. Conversely, the non-dominant members are attracted to the weighted mean of the male population to take advantage of the resources that are wasted by the dominant spiders. Therefore, the update of the positions for the male spiders can be expressed as [40]:

$$\mathbf{M}_i^{k+1} = \begin{cases} \mathbf{M}_i^k + \alpha \cdot Vib_{f_i} \cdot (\mathbf{X}_f - \mathbf{M}_i^k) + \phi \cdot (rand - 0.5) & \omega > \omega_{N_f+m} \\ \mathbf{M}_i^k + \alpha \cdot \left(\sum_{h=1}^{N_m} (\omega_{N_f+h} \cdot \mathbf{M}_i^k) \Big/ \sum_{h=1}^{N_m} \omega_{N_f+h} \right) & \text{else} \end{cases} \tag{6}$$

where $\mathbf{X}_f$ represents the position of the nearest female spider to the ith male spider. $\omega_{N_f} + m$ is the weight of the median spider. $\Sigma_{h=1}{}^{N_m}(\omega_{N_f} + h \cdot \mathbf{M}_i^k)/\Sigma_{h=1}{}^{N_m}\omega_{N_f} + h$ denotes the weighted mean of the male population.

In addition to the above conventional evolutions, the mating operation is performed among the dominant males and their nearby females to increase population diversity. For choosing the females, a mating radius for the male spider is defined as [40]:

$$r = \frac{\sum_{j=1}^{N_d} UB_j - LB_j}{2n} \tag{7}$$

where N_d is the dimension number of the optimization problem. UB_j and LB_j represent the upper and lower bounds of the jth variable, respectively.

The weight of the spider that is involved into the mating operation determines the influence probability to the new spider. Hence, the influence probability of each involved members is assigned by the roulette method, which is formulated as [40]:

$$Ps = \frac{\omega_j}{\sum_{j=1}^{NN} \omega_j} \tag{8}$$

where NN is the number of the involved mating spiders.

It is worth noting that the mating operation will be canceled if there is no female spider located within the range of the mating radius. Once a new spider is generated, it is compared with the spider that possessing the worst fitness to determine whether the worst member is replaced by the new one.

2.2. ISSO algorithms

In the optimization process of the original SSO algorithm, the search history of an individual spider has not been fully utilized. To overcome this shortcoming and take advantage of the useful exploration information, the historical optimal position is added into the ISSO1 model, and the updates of the female and male spiders are defined as:

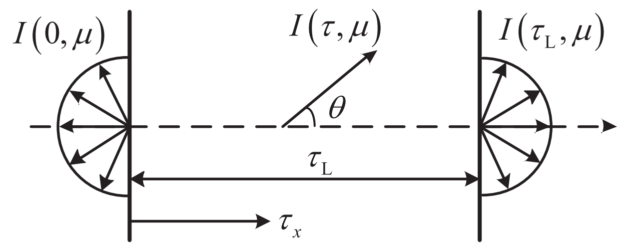

Fig. 3. The physical model of 1D parallel slab.

$$\mathbf{F}_i^{k+1} = \begin{cases} \mathbf{F}_i^k + \alpha \cdot Vib_{c_i} \cdot (\mathbf{X}_c - \mathbf{F}_i^k) + \beta \cdot Vib_{b_i} \cdot (\mathbf{X}_b - \mathbf{F}_i^k) \\ \quad + \varphi \cdot Vib_{h_i} \cdot (\mathbf{X}_h - \mathbf{F}_i^k) + \phi \cdot (rand - 0.5) \quad \delta \le PF \\ \mathbf{F}_i^k - \alpha \cdot Vib_{c_i} \cdot (\mathbf{X}_c - \mathbf{F}_i^k) - \beta \cdot Vib_{b_i} \cdot (\mathbf{X}_b - \mathbf{F}_i^k) \\ \quad - \varphi \cdot Vib_{h_i} \cdot (\mathbf{X}_h - \mathbf{F}_i^k) + \phi \cdot (rand - 0.5) \quad \text{else} \end{cases} \tag{9}$$

$$\mathbf{M}_i^{k+1} = \begin{cases} \mathbf{M}_i^k + \alpha \cdot Vib_{f_i} \cdot (\mathbf{X}_f - \mathbf{M}_i^k) + \varphi \cdot Vib_{h_i} \cdot (\mathbf{X}_h - \mathbf{F}_i^k) + \phi \cdot (rand - 0.5) & \omega > \omega_{N_f+m} \\ \mathbf{M}_i^k + \alpha \cdot \left(\sum_{h=1}^{N_m} (\omega_{N_f+h} \cdot \mathbf{M}_i^k) \middle/ \sum_{h=1}^{N_m} \omega_{N_f+h} \right) & \text{else} \end{cases} \tag{10}$$

where $\mathbf{X}_h$ indicates the best position found by the ith spider so far. φ represents a random number between 0 and 1, and Vib_{h_i} is the vibration

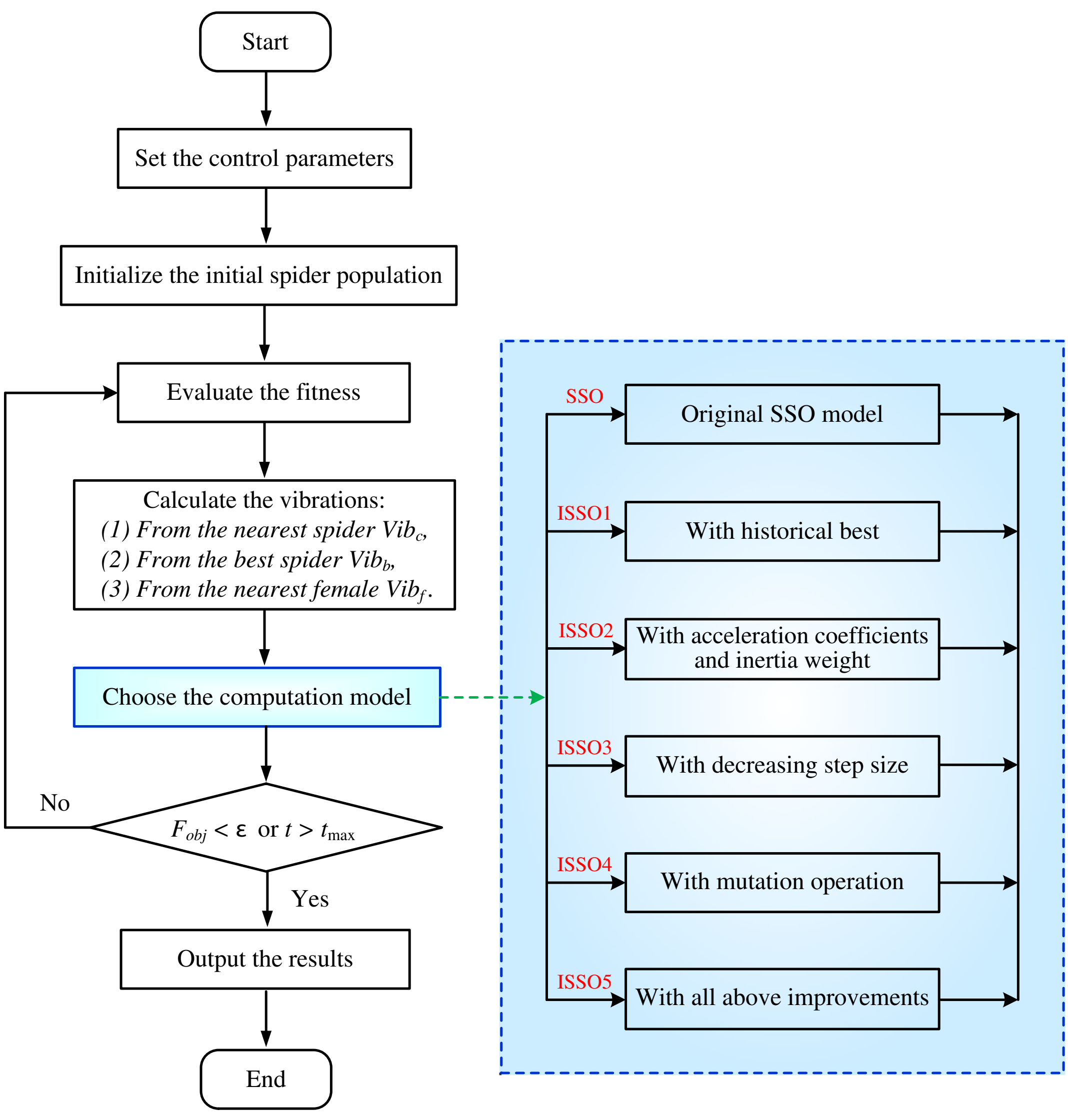

Fig. 2. The flowchart of SSO algorithms.

Table 1
The parameters of the SSO algorithms.

Algorithms	M	PF	UP	LB	ε	$t_{\max}$	$[\chi_1 \sim \chi_6]$	$(\omega_{\max}, \omega_{\min})$	$(\Delta S_{\max}, \Delta S_{\min})$	ω_{PM}
SSO	50	0.7	50	− 50	10^{-9}	1000	–	–	–	–
ISSO1	50	0.7	50	− 50	10^{-9}	1000	–	–	–	–
ISSO2	50	0.7	50	− 50	10^{-9}	1000	[0.3,1.2,0.8,0.6,0.8,0.6]	(1.0,0.05)	–	–
ISSO3	50	0.7	50	− 50	10^{-9}	1000	[0.3,1.2,0.8,0.6,0.8,0.6]	(1.0,0.05)	(1.0,0.3)	–
ISSO4	50	0.7	50	− 50	10^{-9}	1000	–	–		0.3
ISSO5	50	0.7	50	− 50	10^{-9}	1000	[0.3,1.2,0.8,0.6,0.8,0.6]	(1.0,0.05)	(1.0,0.3)	0.3

Table 2
The retrieval results of the radiative source term.

Algorithms	$\overline{a_1} \pm \sigma$	$\overline{\varepsilon_{rel}}\%$	$\overline{a_2} \pm \sigma$	$\overline{\varepsilon_{rel}}\%$	$\overline{a_3} \pm \sigma$	$\overline{\varepsilon_{rel}}\%$
SSO	$2.999 \pm 2.91 \times 10^{-2}$	0.791	$13.992 \pm 3.35 \times 10^{-2}$	0.187	$-13.998 \pm 2.55 \times 10^{-2}$	0.136
ISSO1	$3.001 \pm 8.35 \times 10^{-3}$	0.152	$13.999 \pm 6.56 \times 10^{-3}$	0.066	$-14.001 \pm 9.12 \times 10^{-3}$	0.108
ISSO2	$3.000 \pm 2.43 \times 10^{-3}$	0.064	$14.000 \pm 1.20 \times 10^{-3}$	0.039	$-14.000 \pm 7.39 \times 10^{-3}$	0.049
ISSO3	$3.000 \pm 6.22 \times 10^{-4}$	0.021	$14.000 \pm 4.43 \times 10^{-4}$	0.019	$-14.000 \pm 9.32 \times 10^{-4}$	0.017
ISSO4	$3.000 \pm 5.43 \times 10^{-3}$	0.057	$13.999 \pm 3.14 \times 10^{-3}$	0.058	$-14.001 \pm 8.29 \times 10^{-3}$	0.091
ISSO5	$3.000 \pm 1.95 \times 10^{-4}$	0.005	$14.000 \pm 1.70 \times 10^{-4}$	0.002	$-14.000 \pm 2.75 \times 10^{-4}$	0.002

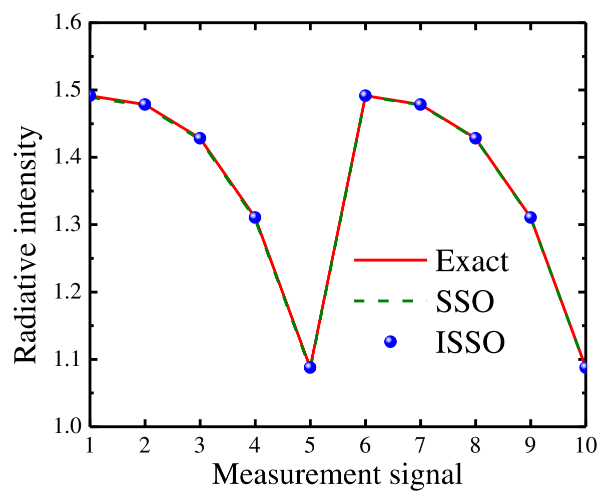

Fig. 4. The comparison between the exact and the reconstructed radiative intensities.

perceived by the ith spider as a result of the influence by the historical optimal position.

Eq. (4) reveals that the greater the distance between two spiders is, the smaller the vibration will be. In the early stage of the search process, distance is usually too wide to provoke an effective vibration to the ith spider, which leads to determining the movements of spiders by the random part and blindfold searches. To overcome the chaotic search of individuals, half of the female spiders and dominant male spiders are randomly selected to be updated as follows:

$$\mathbf{F}_i^{k+1} = \begin{cases} \mathbf{F}_i^k + \alpha \cdot \chi_1 \cdot (\mathbf{X}_c - \mathbf{F}_i^k) + \beta \cdot \chi_2 \cdot (\mathbf{X}_b - \mathbf{F}_i^k) \\ \quad + \varphi \cdot \chi_3 \cdot (\mathbf{X}_h - \mathbf{F}_i^k) + \phi \cdot (rand - 0.5) \quad \delta \le PF \\ \mathbf{F}_i^k - \alpha \cdot \chi_1 \cdot (\mathbf{X}_c - \mathbf{F}_i^k) - \beta \cdot \chi_2 \cdot (\mathbf{X}_b - \mathbf{F}_i^k) - \varphi \cdot \chi_3 \cdot (\mathbf{X}_h - \mathbf{F}_i^k) + \phi \cdot (rand - 0.5) \quad \text{else} \end{cases} \tag{11}$$

$$\mathbf{M}_i^{k+1} = \begin{cases} \mathbf{M}_i^k + \alpha \cdot \chi_4 \cdot (\mathbf{X}_f - \mathbf{M}_i^k) + \varphi \cdot \chi_5 \cdot (\mathbf{X}_h - \mathbf{F}_i^k) + \phi \cdot (rand - 0.5) \quad \omega > \omega_{N_f+m} \\ \mathbf{M}_i^k + \alpha \cdot \chi_6 \cdot \left(\sum_{h=1}^{N_m} (\omega_{N_f+h} \cdot \mathbf{M}_i^k) \Big/ \sum_{h=1}^{N_m} \omega_{N_f+h} \right) \quad \text{else} \end{cases} \tag{12}$$

where χ_1, χ_2, χ_3, χ_4, χ_5, and χ_6 are acceleration coefficients.

Moreover, the last term $\phi \cdot (\text{rand} - 0.5)$ is a random search. Search is less random if the position of the ith spider is excellent. Therefore, the influence of the randomness should be decreased with the increase of iteration number. An inertia weight is introduced to control this influence, which can be defined as:

$$\omega = \omega_{\max} - \frac{t}{t_{\max}} \cdot (\omega_{\max} - \omega_{\min}) \tag{13}$$

where $\omega_{\max}$ and $\omega_{\min}$ are the maximum and minimum values of the inertia weight, respectively. t and $t_{\max}$ denote the present and the maximum iteration numbers, respectively. Hence, the update of spiders in ISSO2 is expressed as:

$$\mathbf{F}_i^{k+1} = \begin{cases} \mathbf{F}_i^k + \alpha \cdot \chi_1 \cdot (\mathbf{X}_c - \mathbf{F}_i^k) + \beta \cdot \chi_2 \cdot (\mathbf{X}_b - \mathbf{F}_i^k) \\ \quad + \varphi \cdot \chi_3 \cdot (\mathbf{X}_h - \mathbf{F}_i^k) + \omega \cdot \phi \cdot (rand - 0.5) \quad \delta \le PF \\ \mathbf{F}_i^k - \alpha \cdot \chi_1 \cdot (\mathbf{X}_c - \mathbf{F}_i^k) - \beta \cdot \chi_2 \cdot (\mathbf{X}_b - \mathbf{F}_i^k) - \varphi \cdot \chi_3 \cdot (\mathbf{X}_h - \mathbf{F}_i^k) \\ \quad + \omega \cdot \phi \cdot (rand - 0.5) \quad \text{else} \end{cases} \tag{14}$$

$$\mathbf{M}_i^{k+1} = \begin{cases} \mathbf{M}_i^k + \alpha \cdot \chi_4 \cdot (\mathbf{X}_f - \mathbf{M}_i^k) + \varphi \cdot \chi_5 \cdot (\mathbf{X}_h - \mathbf{F}_i^k) + \omega \cdot \phi \cdot (rand - 0.5) \quad \omega > \omega_{N_f+m} \\ \mathbf{M}_i^k + \alpha \cdot \chi_6 \cdot \left(\sum_{h=1}^{N_m} (\omega_{N_f+h} \cdot \mathbf{M}_i^k) \Big/ \sum_{h=1}^{N_m} \omega_{N_f+h} \right) \quad \text{else} \end{cases} \tag{15}$$

Moreover, a small step size causes the spiders to search carefully, but the convergence speed is relatively slow. In contrast, a large size of the search step can accelerate convergence, whereas the searches of spiders are rough, which may lead to the spider population missing the optimal position. In ISSO3, a linearly decreased search step size is adopted to make a reasonable trade-off between computation time and computational accuracy, which is defined as:

$$\Delta S = \Delta S_{\max} - \frac{t}{t_{\max}} \cdot (\Delta S_{\max} - \Delta S_{\min}) \tag{16}$$

where $\Delta S_{\max}$ and $\Delta S_{\min}$ represent the maximum and minimum step sizes, respectively.

Hence, the positions of spiders in ISSO3 are updated as follows:

$$\mathbf{F}_i^{k+1} = \begin{cases} \mathbf{F}_i^k + \Delta S \cdot [\alpha \cdot \chi_1 \cdot (\mathbf{X}_c - \mathbf{F}_i^k) + \beta \cdot \chi_2 \cdot (\mathbf{X}_b - \mathbf{F}_i^k) \\ \quad + \varphi \cdot \chi_3 \cdot (\mathbf{X}_h - \mathbf{F}_i^k) + \omega \cdot \phi \cdot (rand - 0.5)] \quad \delta \le PF \\ \mathbf{F}_i^k - \Delta S \cdot [\alpha \cdot \chi_1 \cdot (\mathbf{X}_c - \mathbf{F}_i^k) - \beta \cdot \chi_2 \cdot (\mathbf{X}_b - \mathbf{F}_i^k) - \varphi \cdot \chi_3 \cdot (\mathbf{X}_h - \mathbf{F}_i^k) \\ \quad + \omega \cdot \phi \cdot (rand - 0.5)] \quad \text{else} \end{cases} \tag{17}$$

$$\mathbf{M}_i^{k+1} = \begin{cases} \mathbf{M}_i^k + \Delta S \cdot [\alpha \cdot \chi_4 \cdot (\mathbf{X}_f - \mathbf{M}_i^k) \\ \quad + \varphi \cdot \chi_5 \cdot (\mathbf{X}_h - \mathbf{F}_i^k) + \omega \cdot \phi \cdot (rand - 0.5)] \quad \omega > \omega_{N_f+m} \\ \mathbf{M}_i^k + \alpha \cdot \chi_6 \cdot \left(\sum_{h=1}^{N_m} (\omega_{N_f+h} \cdot \mathbf{M}_i^k) \Big/ \sum_{h=1}^{N_m} \omega_{N_f+h} \right) \quad \text{else} \end{cases} \tag{18}$$

The mating operations among dominant males and females are

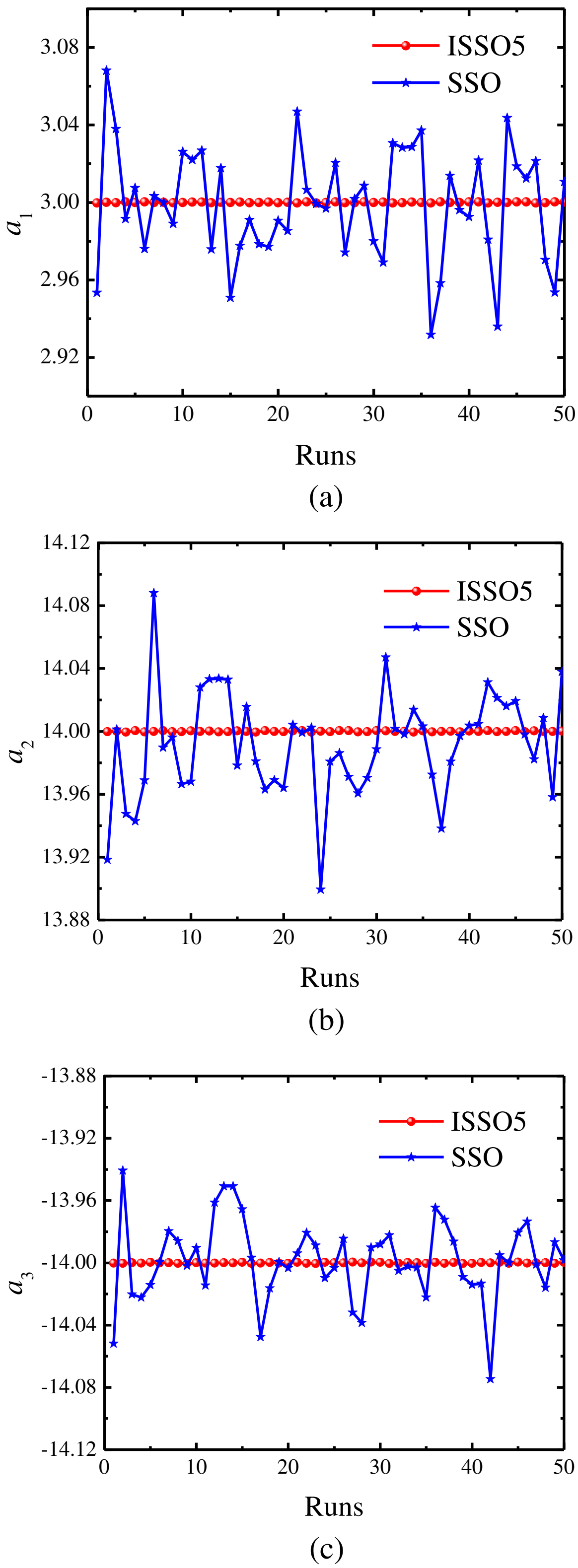

Fig. 5. The retrieval results of (a) a_1, (b) a_2 and (c) a_3 in radiative source term by SSO and ISSO5 algorithms.

applied to increase the diversity of the spider population at each iteration. However, the non-dominant male spiders do not contribute in improving the diversity. Therefore, the mutation operation is executed for non-dominant males in ISSO4, which can be expressed as:

$$\mathbf{M}_i^{k+1} = \begin{cases} \mathbf{M}_{i1}^k + \eta\cdot(\mathbf{M}_{i2}^k - \mathbf{M}_{i3}^k) & \alpha < PM \\ \mathbf{M}_i^k & \text{else} \end{cases} \tag{19}$$

where i_1, i_2, and i_3 are three random integers that are different from i. η denotes the differential evolution amplification coefficient. PM indicates the mutation probability, which can be obtained as follows:

$$PM = \omega_{PM}\cdot\frac{J_i - J_{\text{best}}}{J_{\text{worst}} - J_{\text{best}}} \tag{20}$$

2.3. Calculation procedure

To solve the inverse radiation estimation problems, five ISSO algorithms are tested and compared with the original SSO model, namely: (1) SSO with the influence of the historical optimal position (ISSO1), (2) SSO with acceleration coefficients and linearly decreasing weight (ISSO2), (3) SSO with dynamic changing size of the search step (ISSO3), (4) SSO with mutation operation (ISSO4), and (5) SSO with all the above improvements simultaneously (ISSO5). The main computation procedure of SSO algorithms can be summarized as follows:

Step 1. Structure determination: The control parameters, such as the maximum iteration number, the upper and lower boundaries of variables, and the desired computation accuracy ε, are set.
Step 2. Initialization: The numbers of females and males and the initial spider population are randomly created in the search space.
Step 3. Evaluation: The fitness and weight of each spider are calculated, and the positions and fitness of the best and worst spiders are recorded.
Step 4. Vibration calculation: The vibrations perceived by the female spider from the information transmitted by the nearest and the global best spiders, and the vibration perceived by the male spider from the information conveyed by the nearest female spider are calculated.
Step 5. Improvement: The improved models are selected, and additional information is calculated.
Step 6. Update: The new position of each spider is calculated.
Step 7. Repeat: Step 3 is repeated until one of the following stop criteria is reached: (1) the global best fitness is lower than the desired accuracy, or (2) the iteration number reaches the given maximum iteration number.
Step 8. Output: The computation is stopped, and the retrieved results are output.

The flowchart of the SSO algorithms is described in Fig. 2.

3. Results and discussion

The SSO algorithms including the original SSO and ISSO models are applied to estimate the radiative source term and radiative properties of the medium in inverse transient radiative and coupled radiative–conductive heat transfer problems. Since measurement error is inevitable in the practical researches, the random standard deviation is added into the radiative signals obtained by the direct problem to show the influence of measurement errors on the simulations, which is expressed as:

$$Y_{\text{mea}} = Y_{\text{exa}} + \sigma\varsigma \tag{21}$$

where Y_{mea} and Y_{exa} indicate the measured and exact values of the signals, which are served as input for inverse analysis. ς represents a random variable of normal distribution with zero mean and unit standard deviation. The standard deviations of measured radiative signals, σ for a γ% measured error at 99% confidence, are determined as:

$$\sigma = \frac{Y_{\text{exa}} \times \gamma\%}{2.576} \tag{22}$$

Table 3
The comparison of computational efficiency of SSO algorithms.

Algorithms	Iteration numbers	Computational time [s]	Fitness values
SSO	999.82	$1.9135 \pm 1.82 \times 10^{-3}$	$1.59 \times 10^{-5} \pm 6.64 \times 10^{-5}$
ISSO1	995.52	$1.9078 \pm 1.91 \times 10^{-3}$	$4.16 \times 10^{-6} \pm 3.03 \times 10^{-6}$
ISSO2	889.32	$1.7601 \pm 4.55 \times 10^{-3}$	$1.68 \times 10^{-9} \pm 2.99 \times 10^{-9}$
ISSO3	732.56	$1.3918 \pm 2.19 \times 10^{-3}$	$9.39 \times 10^{-10} \pm 2.07 \times 10^{-10}$
ISSO4	996.44	$1.9071 \pm 1.87 \times 10^{-3}$	$3.39 \times 10^{-7} \pm 8.15 \times 10^{-7}$
ISSO5	559.38	$1.0702 \pm 2.10 \times 10^{-3}$	$3.63 \times 10^{-10} \pm 2.04 \times 10^{-10}$

Table 4
The retrieval results of radiative source term for different measurement errors.

Coeffi-cients	True values	3%		5%		10%		30%	
		$\overline{Y_{est}}$	$\overline{\varepsilon_{rel}}\%$	$\overline{Y_{est}}$	$\overline{\varepsilon_{rel}}\%$	$\overline{Y_{est}}$	$\overline{\varepsilon_{rel}}\%$	$\overline{Y_{est}}$	$\overline{\varepsilon_{rel}}\%$
a_1	3	3.0332	1.1106	3.0534	1.7808	3.0925	3.0836	3.0939	3.1297
a_2	14	13.4955	3.6034	13.1234	6.2612	12.2869	12.2365	8.7836	37.2603
a_3	− 14	− 13.4793	3.7194	− 13.0887	6.5091	− 12.2041	12.8282	− 8.3554	40.3185

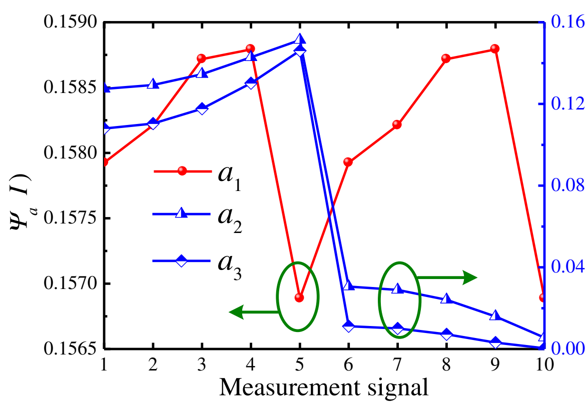

Fig. 6. The sensitivity coefficients of radiative intensity with respect to the coefficients of radiative source term.

where the denominator is set as 2.576, because a normally distributed population is contained within ± 2.576 standard deviation of the mean.

To evaluate the retrieval results, the relative error is defined as:

$$\varepsilon_{rel} = \left| \frac{Y_{est} - Y_{exa}}{Y_{exa}} \right| \times 100\% \tag{23}$$

where Y_{est} denotes the calculated values by the estimated parameters.

Moreover, the sensitivity coefficient is an important parameter for inverse estimation problems which indicates the response of the

Table 5
The parameters of the DOM.

L	β_e	ω	g	ct_p	ct_c	$c\Delta t$	ct
0.5 m	1.0 m^{-1}	0.998	0	1.0 m	3.0 m	0.01 m	10.0 m

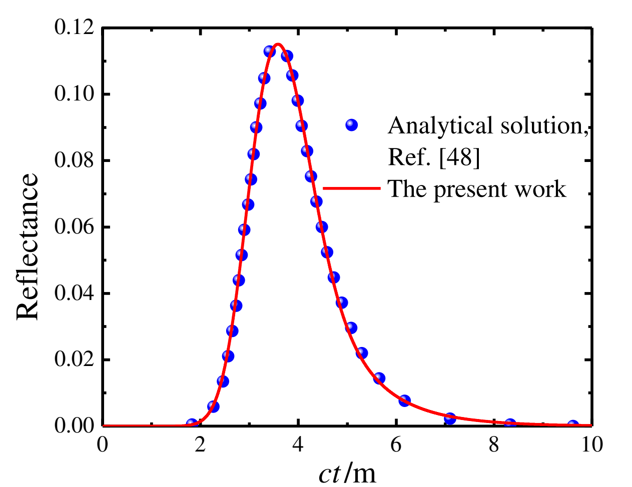

Fig. 8. The validation of the DOM solution for 1D transient radiative heat transfer problems.

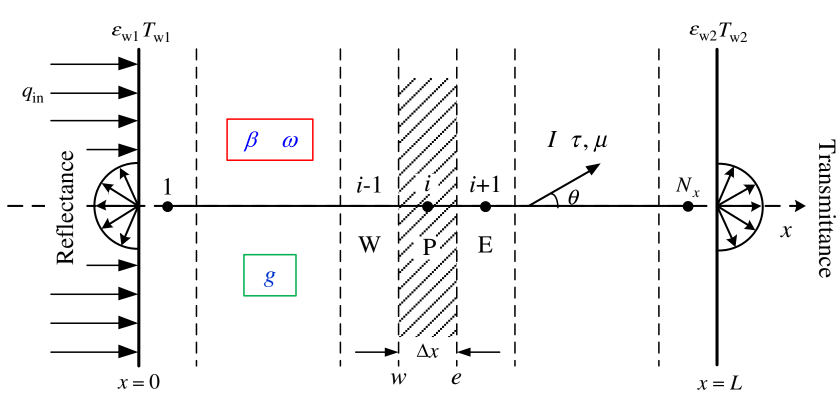

Fig. 7. The schematic of radiative heat transfer in a 1D parallel slab.

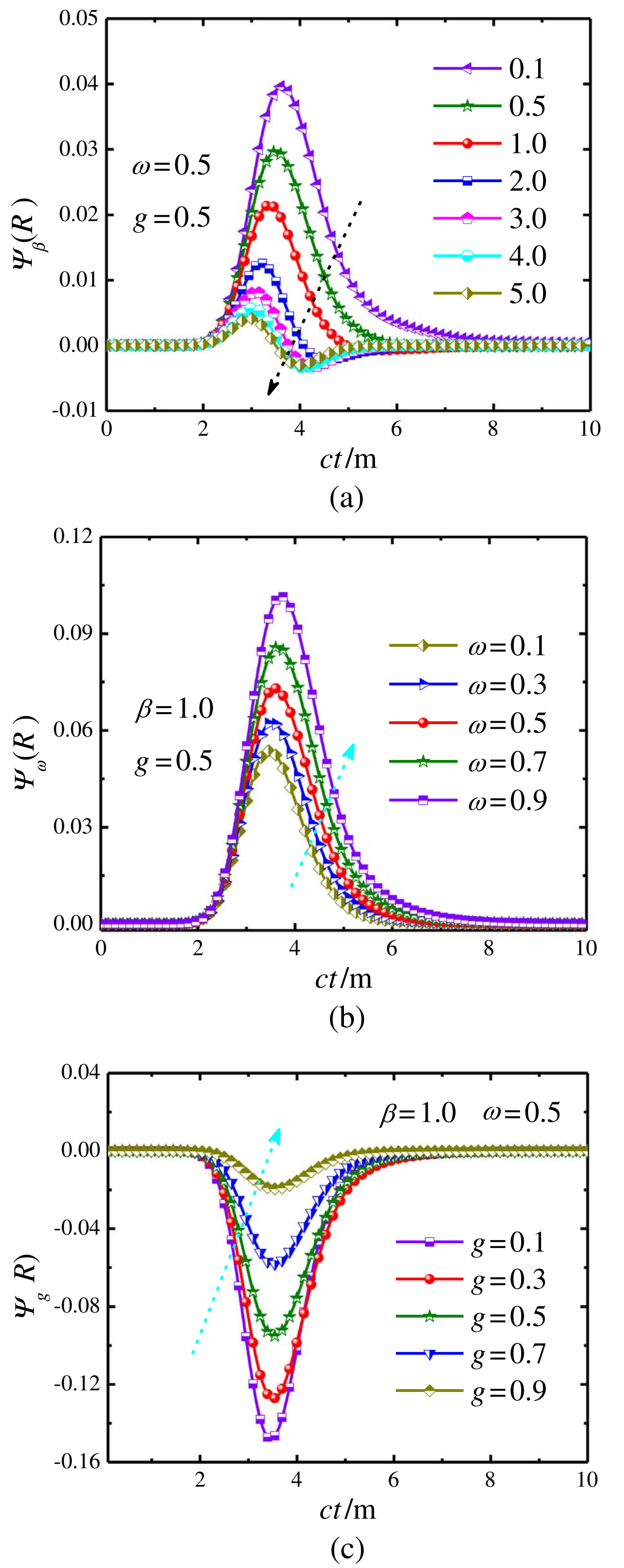

Fig. 9. The sensitivity coefficients of time-resolved reflectance with respect to (a) the extinction coefficient, (b) the scattering albedo and(c) the scattering symmetry factor.

inversion parameters to the changes of the measured signals. A detailed examination of the sensitivity coefficient can also provide considerable insight into the estimation problems. The sensitivity coefficient is defined as:

$$\Psi_{\tilde{p}_i}(m) = \frac{m(\tilde{p}_i + \tilde{p}_i\Delta) - m(\tilde{p}_i - \tilde{p}_i\Delta)}{2\tilde{p}_i\Delta} \tag{24}$$

where m represents the measured values. $\tilde{p}_i$ denotes the value of the ith inverse parameter. $\Psi_{p_i}(m)$ is the sensitivity of m to $\tilde{p}_i$. Δ indicates a fluctuation, which is set as $\Delta = 0.005$ in this study.

All cases are implemented using the Fortran code, and the developed program is executed on an Intel Xeon E7-2680 PC with CPU of Pentium(R) D (2.80 GHz) and 64 GB RAM.

3.1. Inverse estimation for radiation heat transfer problems

3.1.1. Inverse estimation of radiative source term

The radiative source term of 1D plane-parallel gray medium is estimated to verify the feasibility of SSO algorithms in solving inverse radiation heat transfer problems. Moreover, the retrieval results obtained by ISSO algorithms are compared with those obtained by the original SSO to demonstrate the superiority of the improved models.

The physical model of 1D parallel slab is presented in Fig. 3. The radiative intensities can be expressed as [3]:

$$\begin{cases} I^{+}(\tau,\mu) = I_{b1}\exp[(\tau_L\text{-}\tau)/\mu] + \frac{1}{\mu}\int_0^{\tau} S(\tau')\exp[-(\tau\text{-}\tau')/\mu]\mathrm{d}\tau' \quad 0<\mu<1 \\ I^{-}(\tau,\mu) = I_{b2}\exp[(\tau_L\text{-}\tau)/\mu] - \frac{1}{\mu}\int_0^{\tau} S(\tau')\exp[-(\tau\text{-}\tau')/\mu]\mathrm{d}\tau' \\ \qquad -1<\mu<0 \end{cases} \tag{25}$$

with the boundary conditions as follows:

$$\begin{cases} I_{b1} = 0 \\ I_{b2} = 0 \end{cases} \tag{26}$$

$$\begin{cases} \tau = 0 \quad -1 \le \mu \le 0 \\ \tau = \tau_L \quad 0 \le \mu \le 1 \end{cases} \tag{27}$$

where I_{b1} and I_{b2} denote the radiative intensities at the boundaries. τ represents the optical thickness of the medium. μ is the directional cosine, $\mu = \cos\theta$. $S(\tau)$ indicates the radiative source term, which is assumed to be a polynomial function of the optical thickness:

$$S(\tau) = \sum_{i=1}^{N_s} a_i \tau^{i-1} \tag{28}$$

where N_s indicates the number of polynomial in radiative source term.

In this study, the absorption and scattering coefficients of the medium are set as $\kappa_a = 5.0\ \mathrm{m}^{-1}$ and $\kappa_s = 0.0\ \mathrm{m}^{-1}$, respectively. The thickness of the media is set as $L = 1.0$ m. The coefficients in radiative source term is expressed as $\mathbf{a} = [a_1, a_2, \ldots, a_n]^{\mathrm{T}}$, of which exact values are set as $\mathbf{a} = [3, 14, -14]^{\mathrm{T}}$.

The radiative intensities are served as the measured signals for inverse estimation, and the objective function is defined as:

$$F_{\mathrm{obj}} = \sum_{i=1}^{N_n} |I_{\mathrm{est}}(\mathbf{a},\mu,\tau) - I_{\mathrm{cal}}(\mathbf{a},\mu,\tau)| \tag{29}$$

where N_n indicates the number of the measured signals which is set as $N_n = 10$. For the reconstruction results, the average values of the coefficients of radiative source term and relative errors are denoted by $\bar{a}$ and $\overline{\varepsilon_{\mathrm{rel}}}$, respectively.

The SSO algorithms are applied to simulate the coefficients of the radiative source term. The parameters in SSO are listed in Table 1. In view of the random characteristic of intelligent algorithms, all the tests are repeated 50 trials and the estimation results are shown in Table 2. The estimation results reveal that all the improved models are better than the original model, and the ISSO5 algorithm received the best simulation results in terms of standard deviation and relative error. The reconstructed radiative intensities using SSO and ISSO5 algorithms and the corresponding exact values are illustrated in Fig. 4. It is seen that a good agreement between the exact and inversely reconstructed values is obtained.

Table 6
The retrieval results of the extinction coefficient, scattering albedo and scattering symmetry factor.

Algorithms	True values	β_e	$\overline{\varepsilon_{rel}}\%$	ω	$\overline{\varepsilon_{rel}}\%$	g	$\overline{\varepsilon_{rel}}\%$
SSO	$\beta_e = 1.0$	$1.0020 \pm 6.98 \times 10^{-3}$	0.2000	$0.4998 \pm 6.63 \times 10^{-3}$	0.2400	$0.5011 \pm 3.33 \times 10^{-3}$	0.2200
ISSO1	$\omega = 0.5$	$0.9985 \pm 5.11 \times 10^{-3}$	0.1500	$0.5006 \pm 2.19 \times 10^{-3}$	0.1200	$0.4993 \pm 2.01 \times 10^{-3}$	0.1400
ISSO2	$g = 0.5$	$0.9989 \pm 1.25 \times 10^{-3}$	0.1100	$0.4995 \pm 8.90 \times 10^{-4}$	0.1000	$0.5003 \pm 9.43 \times 10^{-4}$	0.0600
ISSO3		$1.0006 \pm 9.36 \times 10^{-4}$	0.0600	$0.5004 \pm 8.25 \times 10^{-4}$	0.0800	$0.5003 \pm 5.61 \times 10^{-4}$	0.0600
ISSO4		$1.0013 \pm 3.16 \times 10^{-3}$	0.1300	$0.4993 \pm 1.55 \times 10^{-4}$	0.1400	$0.5005 \pm 1.17 \times 10^{-3}$	0.1000
ISSO5		$1.0002 \pm 2.59 \times 10^{-4}$	0.0200	$0.5001 \pm 4.33 \times 10^{-4}$	0.0200	$0.4999 \pm 3.40 \times 10^{-4}$	0.0200

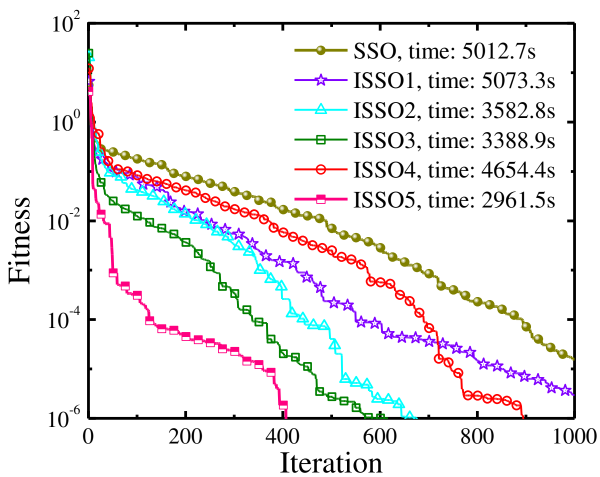

Fig. 10. The fitness function and computation time of the SSO algorithms for simultaneously retrieving the extinction coefficient, scattering albedo and scattering symmetry factor of media.

Fig. 5 shows the comparison between the original SSO and ISSO5 algorithms in solving inverse estimation of radiative source term. The fluctuation of the simulated coefficients in ISSO5 is significantly lesser than those in the original SSO, which demonstrates that the stability of the improved model is also better than the original algorithm.

To further compare the convergence velocity and search ability of SSO algorithms, the iteration numbers, computation time and fitness values of original SSO and ISSO algorithms are listed in Table 3. Evidently, the original model is the most time consuming one, and the objective function in ISSO5 receives the fastest descent speed and the minimum value. According to the above tests, the SSO algorithm is a good candidate for solving inverse radiation problems. Moreover, the proposed improved models possess better performance than the original model in terms of computation accuracy, convergence velocity and stability, and the ISSO5 algorithm is the best one.

To test the tolerance of the SSO algorithm in solving optimization tasks, large measurement errors are added to the measured signals. Table 4 lists the retrieval results of radiative source term for different measurement errors. As shown, the maximum relative error of a_3 has reached more than 40% whereas the relative error of a_1 is only 3.13%, which mainly due to radiative intensities are more sensitive to the latter. The sensitivity coefficients of exit radiative intensities with respect to the coefficients of radiative source term are illustrated in Fig. 6.

3.1.2. Inverse estimation of optical parameters and scattering phase function of the medium

The 1D transient radiative heat transfer problem filled with participating medium is described here. Fig. 7 illustrates that the left boundary is exposed to a pulse laser irradiation, and both sides are assumed to be diffuse and gray walls. The 1D TRTE can be expressed as [3]:

$$\frac{n}{c}\frac{\partial I(x,\mathbf{s},t)}{\partial t} + \frac{\partial I(x,\mathbf{s},t)}{\partial x} = -\beta_e I(x,\mathbf{s},t) + n^2\kappa_a I_b(x,t) + \frac{\kappa_s}{4\pi}\int_{4\pi} I(x,\mathbf{s}',t)\Phi(\mathbf{s}',\mathbf{s})\mathrm{d}\Omega' \tag{30}$$

where n is the refractive index. β_e is the extinction coefficient. The scattering albedo can be denoted by $\omega = \kappa_s/\beta_e$. $\mathbf{s}'$ and $\mathbf{s}$ indicate the incident and the scattering directions, respectively. $\Phi(\mathbf{s}',\mathbf{s})$ represents the scattering phase function, and an H–G scattering phase function is considered here, which is defined as:

$$\Phi(\mathbf{s}',\mathbf{s}) = \frac{1-g^2}{[1+g^2-2g\cdot\cos(\mathbf{s}'-\mathbf{s})]^{3/2}} \tag{31}$$

where g is the scattering asymmetry factor.

The radiative intensity can be expressed as:

$$I(x,\mathbf{s},t) = I_c(x,\mathbf{s},t) + I_d(x,\mathbf{s},t) \tag{32}$$

where I_c and I_d represent the diffused radiative intensity that scattered from the radiative source and the remaining collimated radiative intensity. Hence, the TRTE can be expressed as:

$$\begin{aligned}&\frac{n}{c}\left[\frac{\partial I_c(x,\mathbf{s},t)}{\partial t} + \frac{\partial I_d(x,\mathbf{s},t)}{\partial t}\right] + \left[\frac{\partial I_c(x,\mathbf{s},t)}{\partial x} + \frac{\partial I_d(x,\mathbf{s},t)}{\partial x}\right]\\ &= -\beta_e[I_c(x,\mathbf{s},t) + I_d(x,\mathbf{s},t)] + n^2\kappa_a I_b(x,t)\\ &\quad + \frac{\kappa_s}{4\pi}\int_{4\pi}[I_c(x,\mathbf{s}',t) + I_d(x,\mathbf{s}',t)]\Phi(\mathbf{s},\mathbf{s}')\mathrm{d}\Omega'\end{aligned} \tag{33}$$

For the collimated radiative intensity, the relationship at position x and time t in direction $\mathbf{s}$ can be expressed as:

$$\frac{n}{c}\frac{\partial I_c(x,\mathbf{s},t)}{\partial t} + \frac{\partial I_c(x,\mathbf{s},t)}{\partial x} = -\beta_e I_c(x,\mathbf{s},t) \tag{34}$$

The solution for the Eq. (33) can be expressed as:

$$I_c(x,\mathbf{s},t) = I_{in}\left(t - \frac{x}{c}\right)\cdot\boldsymbol{\delta}(\mathbf{s}'-\mathbf{s})\cdot\exp(-\beta_e x) \tag{35}$$

where $\boldsymbol{\delta}$ is the Dirac's delta function. I_{in} indicates the radiative intensity that incident on the left boundary. In this section, the incident radiative intensity follows the Gaussian distribution, which is presented as:

Table 7
The simultaneous estimation results of the ISSO5 algorithm with different measurement errors.

Parameters	True values	γ = 0%		γ = 1%		γ = 3%		γ = 5%	
		ISSO5	ε_{rel}(%)	ISSO5	ε_{rel}(%)	ISSO5	ε_{rel}(%)	ISSO5	ε_{rel}(%)
β_e	1.0	1.0004	0.0400	0.9923	0.7700	0.9846	1.5400	0.9785	2.1500
ω	0.5	0.5003	0.0600	0.5039	0.7800	0.5088	1.7600	0.5104	2.0800
g	0.5	0.4998	0.0400	0.4977	0.4600	0.4936	1.2800	0.4910	1.8000

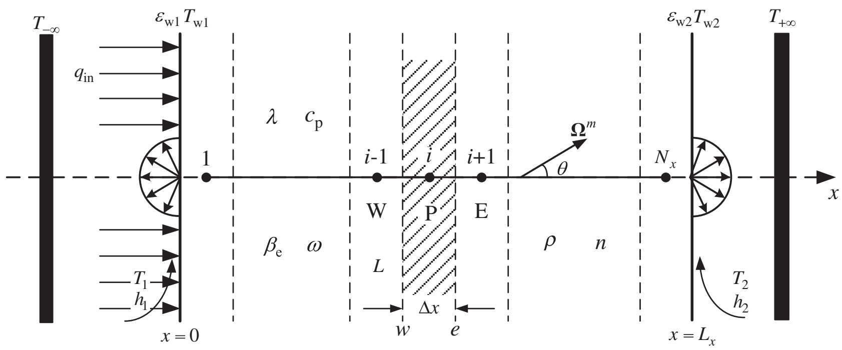

Fig. 11. The schematic of the coupled radiation-conduction heat transfer in a 1D parallel slab.

Table 8
The parameter settings in the 1D transient radiation-conduction heat transfer problems.

Parameters	Nomenclature	Unit	Case 1	Case 2
Thickness of the medium	L	m	0.01	0.01
Thermal conductivity	λ	W/(m·K)	0.7	0.7
Convective heat transfer coefficient	h_w	W/(m^2·K)	7.0	7.0
Specific heat capacity at constant volume	$c_v = \rho c_p$	J/(m^3·K)	2.2×10^6	2.2×10^6
Power density of the incident laser	q_{in}	W/m^2	50,000	50,000
Ambient temperature	T_s	K	300	300
Extinction coefficient	β_e	m^{-1}	1.0	30.0
Scattering albedo	ω	–	0.0	0.0
Refraction index	n	–	1.5	1.5
Time step	Δt	s	0.1	0.1
Pulse laser width	ct_q	m	1.0	1.0
Scattering phase function	Φ	–	1.0	1.0

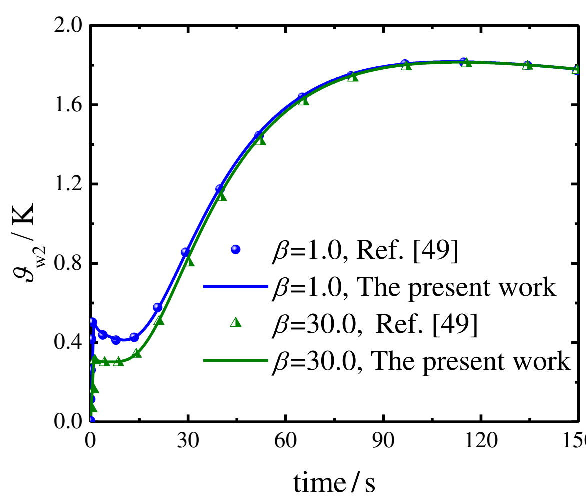

Fig. 12. The validation of the DOM solution for 1D transient coupled radiation-conduction heat transfer problems.

Table 10
The definitions of dimensionless variables in the coupled radiation-conduction heat transfer problems.

Parameters	Θ	τ	N_{cr}	h^*	$q_r{}^*$	$q_{in}{}^*$	I^*	t^*
Expressions	$\frac{T}{T_s}$	$\beta_e x$	$\frac{\lambda\beta_e}{4n^2\sigma T_s^3}$	$\frac{h}{4n^2\sigma T_s^3}$	$\frac{q_r}{4n^2\sigma T_s^4}$	$\frac{q_{in}}{4n^2\sigma T_s^4}$	$\frac{\pi I}{\sigma T_s^4}$	$\frac{\lambda\beta^2 t}{\rho c_p}$

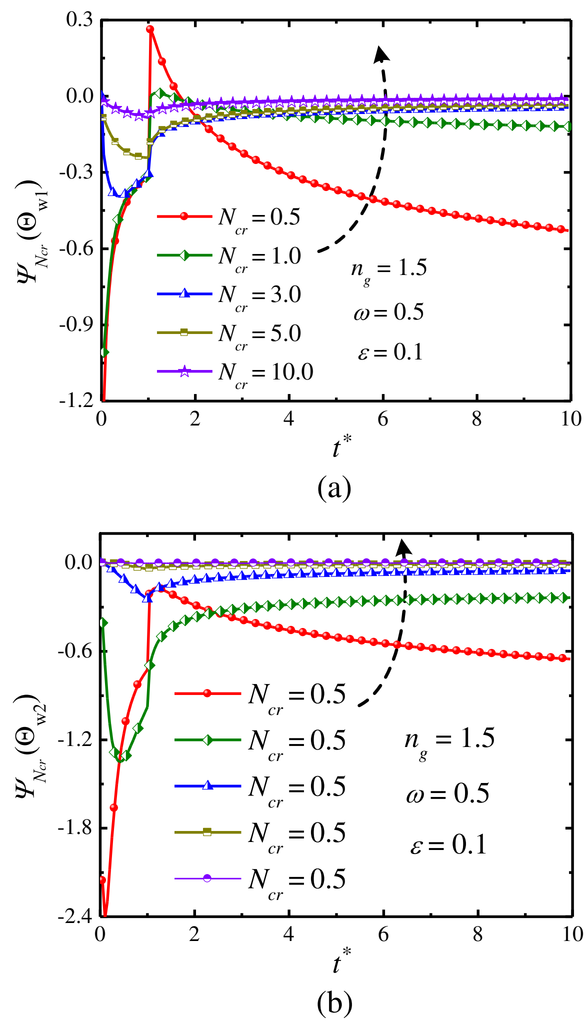

Fig. 13. The sensitivity coefficients of the dimensionless temperatures on the (a) left boundary and (b) right boundary with respect to the conduction-radiation parameter.

$$\begin{cases} I_{in} = I_0 \exp\left[-4\ln\left(\frac{t-t_c}{t_p}\right)^2\right] & 0 < t < 2t_c \\ I_{in} = 0 & \text{else} \end{cases} \tag{36}$$

Thus, TRTE can be expressed as:

$$\frac{n}{c}\frac{\partial I_d(x,\mathbf{s},t)}{\partial t} + \frac{\partial I_d(x,\mathbf{s},t)}{\partial x} = -\beta_e I_d(x,\mathbf{s},t) + \frac{\kappa_s}{4\pi}\int_{4\pi}[I_c(x,\mathbf{s}',t) + I_d(x,\mathbf{s}',t)]\Phi(\mathbf{s},\mathbf{s}')\mathrm{d}\Omega' \tag{37}$$

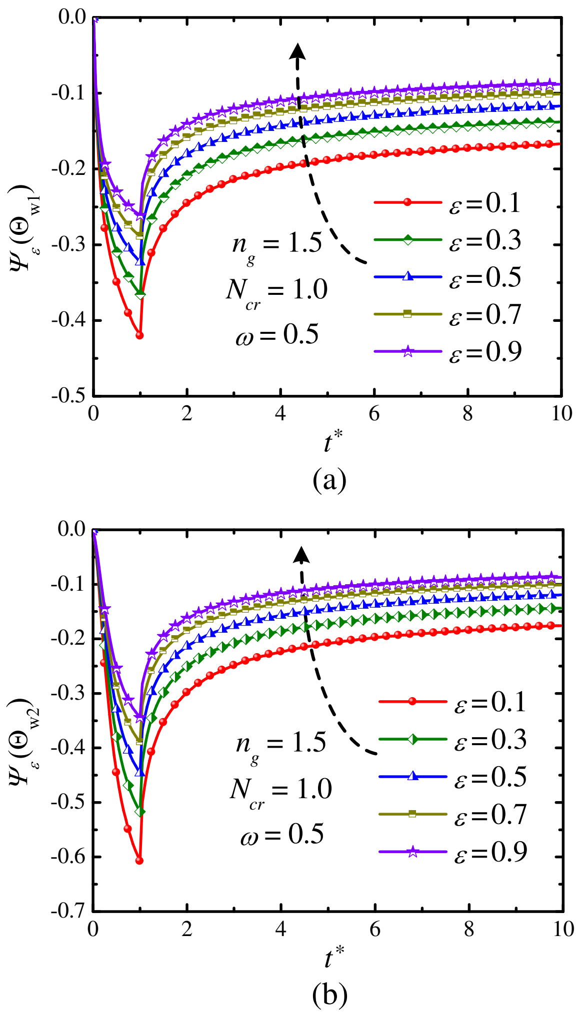

Fig. 14. The sensitivity coefficients of the dimensionless temperatures on the (a) left and (b) right boundaries with respect to the boundary emissivity.

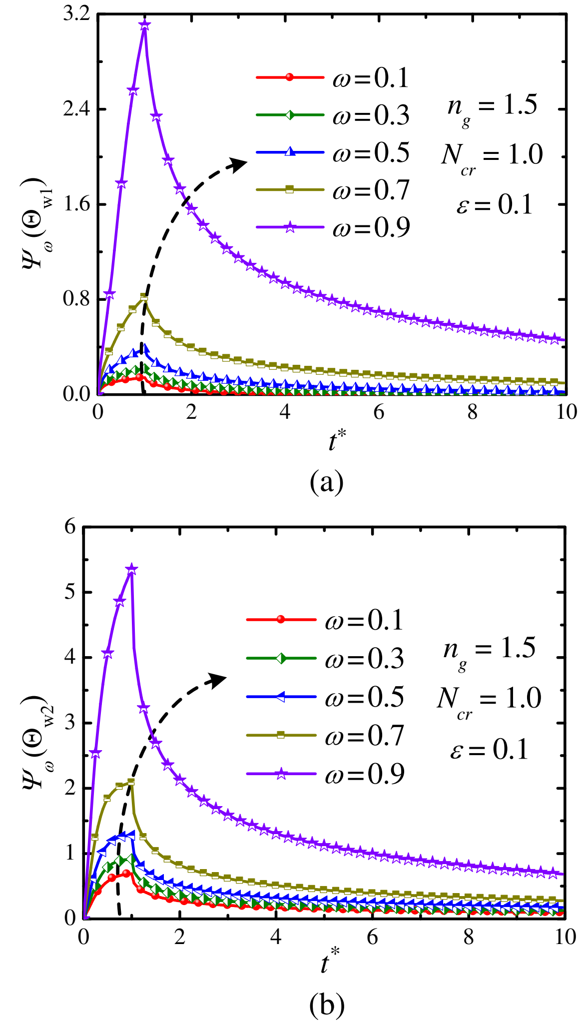

Fig. 15. The sensitivity coefficients of the dimensionless temperatures on the (a) left and (b) right boundaries with respect to the scattering albedo.

The initial condition of the radiation problem is given as:

$$I(x, \mathbf{s}, 0) = 0 \tag{38}$$

Moreover, the boundary conditions for the TRTE are given as follows:

$$I(0, \mathbf{s}, t) = 0 \quad \mu > 0 \tag{39}$$

$$I(L, \mathbf{s}, t) = 0 \quad \mu < 0 \tag{40}$$

The DOM is applied to solve TRTE. For simplicity, the details of DOM for solving radiation problems have been introduced in Ref. [47] and are not repeated here. A radiative heat transfer problem for 1D slab filled with absorbing and scattering medium is tested to validate the accuracy of DOM codes. The related parameters are listed in Table 5, and the convergence criterion is set as $\varepsilon = 10^{-6}$. The simulated reflectance is compared with the results in Ref. [48], which is shown in Fig. 8. The retrieval results demonstrate the reliability of the DOM codes.

Fig. 8 illustrates that the time-dependent reflectance tends to be 0 at the beginning and ending stages. To collect the most effective information for inverse analysis, the objective function is defined as:

$$F_{\mathrm{obj}} = \sum_{t=t_1}^{t_2} \left[1 - \frac{R_{\mathrm{est}}(\beta_{\mathrm{e}}, \omega, g, t)}{R_{\mathrm{cal}}(\beta_{\mathrm{e}}, \omega, g, t)} \right]^2 \tag{41}$$

where R_{est} and R_{cal} represent the estimated reflectance and the calculated reflectance according to the exact optical properties, respectively. The time interval $[t_1, t_2]$ satisfies $ct \in [2\ \mathrm{m}, 8\ \mathrm{m}]$.

The H–G scattering phase function is considered in this section, and the SSO algorithms are applied to estimate the extinction coefficient, scattering albedo and scattering symmetry factor of the medium simultaneously. Predicting the scattering phase function is more sensitive to the measurement error than the optical parameters, which results in a greater difficulty for simultaneously retrieving the coefficient g and the optical parameters. Fig. 9 shows the coefficients of the reflectance signals with respect to the estimation parameters. As shown, the absolute values of sensitivity coefficient are positively correlated with the scattering albedo, while negatively correlated with the extinction coefficient and the phase function coefficient. Therefore, a relatively small extinction coefficient, and large scattering albedo and phase function coefficient are beneficial to the inverse estimation for the three parameters. The iteration stops until one of the following conditions is satisfied: (1) the fitness value is less than the convergence accuracy $\varepsilon = 10^{-6}$, and (2) the iteration number reaches the maximum value

Table 11
The parameters of the inverse radiation-conduction heat transfer problems.

Parameters	q_{in}^*	n	τ	t^*	Δt	t_q	ε	$t_{\max}$
Values	500	1.5	1.0	0.008	0.00005	0.001	10^{-6}	500

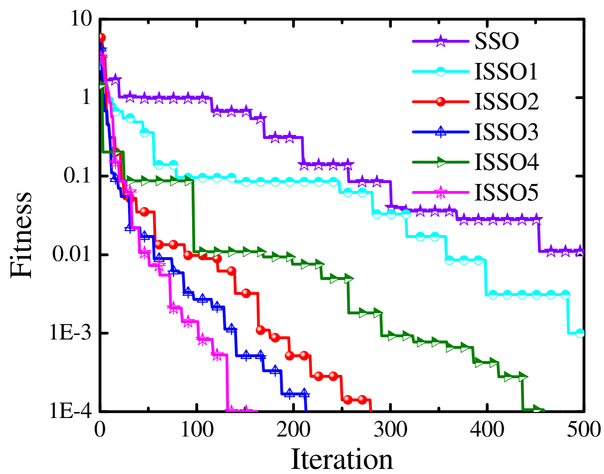

Fig. 16. The fitness function of the SSO algorithms for the inverse radiation-conduction heat transfer problems.

$t_{max} = 1000$.

Table 6 lists the reconstruction results of these three parameters and Fig. 10 shows the iteration numbers and computation time by using original SSO and ISSO algorithms. As shown, ISSO algorithms are more effective than the original SSO model, and ISSO5 algorithm is the fastest one. The absolute errors and variances of the extinction coefficient are greater than those of the scattering symmetry factor and scattering albedo, which mainly due to reflectance on the boundary is less sensitive to the former.

Table 7 lists the simultaneous estimation results of ISSO5 algorithm for different measurement errors. All the parameters are accurately reconstructed even with a noisy data, and the maximum relative error is only 2.15% when the measurement error reached 5%.

It is worth noting that the proposed SSO algorithm is also applicable for simultaneously retrieving more parameters. One spider in the SSO algorithm represents a potential solution of the inverse problem. The parameters needed to be retrieved indicate one dimension of a spider's position $\boldsymbol{X}(x_1, x_2 \ldots x_n)$. Therefore, if more than three parameters needed to be estimated at a time, we just need to add an additional dimension to the spider's position. In addition, different search strategies based on the gender of spider individual can keep the spider swarm from trapping into the local optimum, which significantly enhance the search ability of spider population, especially for solving multi-parameter estimation problems.

3.2. Inverse estimation for radiation–conduction heat transfer problems

In this section, a problem of transient coupled radiation–conduction heat transfer problem is considered. Fig. 11 shows that the 1D slab is located between two black surfaces with temperatures $T_{-\infty}$ and $T_{+\infty}$. The two surfaces of the slab are black opaque walls, and the left boundary is exposed to the collimated pulse laser. In comparison with the radiative heat transfer problems, the temperature distribution is unknown in coupled radiation–conduction model, which can be obtained by the following energy equation:

$$\rho c_p \frac{\partial T}{\partial t} = \lambda \frac{\partial^2 T}{\partial x^2} - \frac{\partial q_r}{\partial x} \tag{42}$$

where ρ represents the density of the medium. c_p denotes the specific heat capacity at constant pressure of the medium. T is temperature. q_r. indicates the radiative source term. The boundary conditions are defined as:

$$-\lambda \frac{\partial T(0,\ t)}{\partial x} = \varepsilon_{w1} q_{in} + \varepsilon_{w1}\sigma(T_s^4 - T_{w1}^4) + \varepsilon_{w1}(q_{w1}^r - \sigma T_{w1}^4) + h_{\ 1}(T_s - T_{w1}) \tag{43}$$

$$\lambda \frac{\partial T(L,\ t)}{\partial x} = \varepsilon_{w2}\sigma(T_s^4 - T_{w2}^4) + \varepsilon_{w2}(q_{w1}^r - \sigma T_{w2}^4) + h_{\ 2}(T_s - T_{w2}) \tag{44}$$

where ε_{w1} and ε_{w2} denote the emissivity of the left and right boundaries, respectively. q_{in} indicates the power density of the incident laser. σ represents the Stefan–Boltzmann constant. T_s is the ambient temperature. h_1 and h_2 convective heat transfer coefficients on the left and right boundaries, and temperature of the boundaries are denoted by T_{w1} and T_{w2}, respectively.

The TRTE is also expressed by the Eq. (30), but the boundary conditions for the coupled radiation–conduction problems should be different. The boundary conditions for the opaque and diffuse surfaces are expressed as:

$$I_{w1} = n^2 \varepsilon I_{b,w1} + \frac{1 - \varepsilon_{w1}}{\pi} \int_{\mathbf{n}_{w1}\cdot\mathbf{s}' < 0} I_{w1}(x, \mathbf{s}')\ |\mathbf{n}_{w1}\cdot\mathbf{s}'|\, d\Omega' \tag{45}$$

$$I_{w2} = n^2 \varepsilon I_{b,w2} + \frac{1 - \varepsilon_{w2}}{\pi} \int_{\mathbf{n}_{w2}\cdot\mathbf{s}' < 0} I_{w2}(x, \mathbf{s}')\ |\mathbf{n}_{w2}\cdot\mathbf{s}'|\, d\Omega' \tag{46}$$

where $\mathbf{n}_{w1}$ and $\mathbf{n}_{w2}$ represent the outward normal vectors on the left and right boundaries, respectively.

The excess temperature on the boundary is defined as:

$$\vartheta_w = T_w - T_s \tag{47}$$

The DOM is applied to solve the direct problems, and two cases of coupled radiation–conduction heat transfer are executed to verify the feasibility of DOM codes. The related parameters are listed in Table 8, and the retrieval excess temperature is compared to that obtained by the ray tracing method in Ref. [49], which is illustrated in Fig. 12. As shown, the retrieval results are consistent with those by ray tracing method.

The SSO algorithms are applied to solve the inverse estimation of the extinction coefficient, scattering albedo, and thermal conductivity in transient coupled radiation–conduction problems. The physical parameters are transformed into dimensionless form to facilitate the subsequent analysis, which are listed in Table 10.

The dimensionless energy equation and its boundary conditions can be expressed as:

$$\frac{\partial \Theta}{\partial t^*} = \frac{\partial^2 \Theta}{\partial \tau^2} - \frac{1}{N_{cr}} \frac{\partial q_r^*}{\partial \tau} \tag{48}$$

Table 12
The retrieval results of the conduction-radiation parameter, the boundary emissivity and the scattering albedo by different SSO algorithms.

Algorithms	N_{cr}	$\overline{\varepsilon_{rel}}\%$	ε	$\overline{\varepsilon_{rel}}\%$	ω	$\overline{\varepsilon_{rel}}\%$
SSO	$1.0031 \pm 6.14 \times 10^{-3}$	0.3100	$0.5022 \pm 8.21 \times 10^{-3}$	0.4400	$0.0991 \pm 7.15 \times 10^{-3}$	0.9000
ISSO1	$1.0014 \pm 2.59 \times 10^{-3}$	0.1400	$0.4991 \pm 6.54 \times 10^{-3}$	0.1800	$0.1007 \pm 5.57 \times 10^{-3}$	0.7000
ISSO2	$1.0008 \pm 8.93 \times 10^{-4}$	0.0800	$0.5006 \pm 1.02 \times 10^{-3}$	0.1200	$0.1003 \pm 2.68 \times 10^{-3}$	0.3000
ISSO3	$0.9998 \pm 4.14 \times 10^{-4}$	0.0200	$0.4996 \pm 6.99 \times 10^{-4}$	0.0800	$0.1003 \pm 9.11 \times 10^{-4}$	0.3000
ISSO4	$0.9993 \pm 3.10 \times 10^{-3}$	0.0700	$0.5008 \pm 4.36 \times 10^{-3}$	0.1600	$0.0994 \pm 6.46 \times 10^{-3}$	0.6000
ISSO5	$1.0000 \pm 6.92 \times 10^{-5}$	0.0000	$0.5001 \pm 2.33 \times 10^{-4}$	0.0200	$0.1000 \pm 3.24 \times 10^{-5}$	0.0000

Table 13
The retrieval results of the ISSO5 algorithm with different measurement errors.

Parameters	True values	γ = 0%		γ = 1%		γ = 3%		γ = 5%	
		ISSO5	ε_{rel}(%)	ISSO5	ε_{rel}(%)	ISSO5	ε_{rel}(%)	ISSO5	ε_{rel}(%)
N_{cr}	1.0	1.0001	0.0100	0.9996	0.0400	0.9989	0.1100	0.9975	0.2500
ω	0.5	0.5001	0.0200	0.5017	0.3400	0.5033	0.6600	0.5103	2.0600
ε	0.1	0.1000	0.0000	0.1007	0.7000	0.1022	2.2000	0.1027	2.7000

$$-N_{cr}\frac{\partial\Theta}{\partial\tau}=\varepsilon_{\mathrm{w1}}q_{\mathrm{in}}^{*}+\frac{\varepsilon_{\mathrm{w1}}}{4n^2}(1-\Theta_{\mathrm{w1}}^4)+\varepsilon_{\mathrm{w1}}\left(q_{\mathrm{w1}}^{\mathrm{r}\ *}-\frac{1}{4n^2}\Theta_{\mathrm{w1}}^4\right)+h_1^*(1-\Theta_{\mathrm{w1}}) \tag{49}$$

$$N_{cr}\frac{\partial\Theta(L,\ t)}{\partial\tau}=\frac{\varepsilon_{\mathrm{w2}}}{4n^2}(1-\Theta_{\mathrm{w2}}^4)+\varepsilon_{\mathrm{w2}}\left(q_{\mathrm{w2}}^{\mathrm{r}\ *}-\frac{1}{4n^2}\Theta_{\mathrm{w2}}^4\right)+h_2^*(1-\Theta_{\mathrm{w2}}) \tag{50}$$

The dimensionless TRTE and its boundary conditions can be written as:

$$\frac{n}{c\beta T_{\mathrm{s}}}\frac{\partial I(x,\mu,t)}{\partial t^*}+\frac{\partial I^*(\tau,\mu,t^*)}{\partial\tau}=-I^*(\tau,\mu,t^*)+n^2(1-\omega)\Theta^4+\frac{\omega}{4\pi}\int_{4\pi}I^*(\tau,\mu,t^*)\Phi(\mu,\mu')\mathrm{d}\Omega \tag{51}$$

$$I_{\mathrm{w1}}^*=n^2\varepsilon_{\mathrm{w1}}\Theta_{\mathrm{w1}}^4I_{\mathrm{b,w1}}+\frac{1-\varepsilon}{\pi}\int_{\mathbf{n}_{\mathrm{w1}}\cdot\Omega'}I_{\mathrm{w1}}^*\ |\mathbf{n}_{\mathrm{w1}}\cdot\Omega'|\,\mathrm{d}\Omega' \tag{52}$$

$$I_{\mathrm{w2}}^*=n^2\varepsilon_{\mathrm{w2}}\Theta_{\mathrm{w2}}^4I_{\mathrm{b,w2}}+\frac{1-\varepsilon}{\pi}\int_{\mathbf{n}_{\mathrm{w2}}\cdot\Omega'}I_{\mathrm{w2}}^*\ |\mathbf{n}_{\mathrm{w2}}\cdot\Omega'|\,\mathrm{d}\Omega' \tag{53}$$

According to the above dimensionless equations, three physical parameters, namely the conduction–radiation parameter, the medium albedo, and the surface emissivity, have a direct influence on the dimensionless temperature of the boundary at a definite time. SSO algorithms are used to estimate the three parameters, and the time-resolved dimensionless temperatures on the boundaries are served as input for the inverse analysis. The objective function is defined as:

$$F_{\mathrm{obj}}=\frac{1}{2}\sum_t\left[\left(1-\frac{\Theta_{\mathrm{w1,est}}}{\Theta_{\mathrm{w1,mea}}}\right)^2-\left(1-\frac{\Theta_{\mathrm{w2,est}}}{\Theta_{\mathrm{w2,mea}}}\right)^2\right] \tag{54}$$

where $\Theta_{\mathrm{est.}}$ and Θ_{mea} represent the estimated and measured dimensionless temperature, respectively. Θ_{w1} and Θ_{w2} are the dimensionless temperatures on the left and right boundaries, respectively. The sensitivity coefficients for the dimensionless temperatures on the boundaries with respect to the conduction-radiation parameter, boundary emissivity and scattering albedo are illustrated in Figs. 13, 14 and 15, respectively. As shown, the sensitivity coefficients of the dimensionless temperature on the boundaries are negatively correlated with the conduction–radiation parameter and the boundary emissivity, whereas positively correlated with the scattering albedo. According to the sensitivity analysis, selecting the similar orders of magnitude for the three parameters is beneficial to the inverse estimation tasks.

The exact values of the inversion parameters are set as $\mathbf{a}=[N_{cr},\ \varepsilon,\ \omega]^{\mathrm{T}}=[1.0,\ 0.5,\ 0.1]^{\mathrm{T}}$, and the other parameter settings are listed in Table 11. Fig. 16 shows the fitness values of different SSO algorithms. ISSO5 algorithm received the fastest convergence velocity for the inverse estimation problems. The retrieval results of the parameters are listed in Table 12. As shown, all the parameters are accurately estimated by SSO algorithms, and the relative error obtained by the ISSO5 algorithm is lower than that obtained by any other methods.

The measurement errors are added into the measured signals to further illustrate the performance of the SSO algorithm, and different extinction coefficients, scattering albedos, and thermal conductivities are estimated simultaneously. Table 13 shows that all the parameters are accurately retrieved even with the measurement errors, and the highest relative error is only 2.70% when the measurement error is increased to 5%.

It is worth noting that the proposed SSO algorithm is also applicable for simultaneously retrieving more parameters because lots of feasible solutions can be processed in parallel at each iteration. In addition, different search strategies based on the gender of spider individual can keep the spider swarm from trapping into the local optimum, which significantly enhance the search ability of spider population, especially for solving multi-parameter estimation problems.

4. Conclusions

The novel bio-inspired swarm algorithm SSO is introduced to solve the estimation problems of inverse transient radiation and coupled radiation–conduction for the first time. Based on the original SSO algorithm, five ISSO algorithms are developed to accelerate the convergence velocity and the global search ability of the inverse model. Furthermore, the SSO algorithms are applied to solve the inverse estimation problems in a 1D participating medium. The sensitivity analysis of the measured signals with respect to the physical parameters of the medium are described initially. Subsequently, the radiative source term, extinction coefficient, scattering albedo, and scattering symmetry factor in the radiation heat transfer problems and the conduction–radiation parameter, boundary emissivity, and scattering albedo in the coupled radiation–conduction heat transfer problems are retrieved. All the parameters are accurately reconstructed by the SSO algorithms even with noisy data. The retrieval results show that the ISSO algorithms possess better performance than the original SSO model in terms of computational accuracy and convergence velocity. The further research direction is to solve the inverse estimation tasks in multidimensional multi-parameter problems of coupled conduction–radiation heat transfer with phase change and the inverse design problems of radiative enclosures by means of SSO algorithms.

Acknowledgements

The support of this work by the National Natural Science Foundation of China (No. 51576053, 51476043) and the Foundation for Innovative Research Groups of the National Natural Science Foundation of China (No. 51421063) are gratefully acknowledged. A very special acknowledgement is made to the editors and referees who make important comments to improve this paper.

References

[1] N.J. McCormick, Inverse radiative transfer problems: a review, Nucl. Sci. Eng. 112 (3) (1992) 185–198.
[2] M.N. Özisik, H.R.B. Orlande, Inverse Heat Transfer: Fundamentals and Applications, CRC Press, Boca Raton, 2000.
[3] M.F. Modest, Radiative Heat Transfer, Academic Press, New York, 2013.
[4] H.P. Tan, B. Maestre, M. Lallemand, Transient and steady-state combined heat transfer in semi-transparent materials subjected to a pulse or a step irradiation, ASME J. Heat Transfer 113 (1) (1991) 166–173.
[5] H.R.B. Orlande, Inverse problems in heat transfer: new trends on solution methodologies and applications, ASME J. Heat Transfer 134 (3) (2012) 031011.
[6] H.P. Tan, P.Y. Wang, X.L. Xia, Transient coupled radiation and conduction in an absorbing and scattering composite layer, AIAA J. Thermophys. Heat Transfer 14 (1) (2000) 77–87.
[7] L.H. Liu, Simultaneous identification of temperature profile and absorption coefficient in one-dimensional semitransparent medium by inverse radiation analysis, Int.

Commun. Heat Mass Transfer 27 (5) (2000) 635–643.
[8] H.Y. Li, M.N. Ozisik, Inverse radiation problem for simultaneous estimation of temperature profile and surface reflectivity, J. Thermophys. Heat Transf. 7 (1) (1993) 88–93.
[9] M. Cui, X.W. Gao, J.B. Zhang, A new approach for the estimation of temperature-dependent thermal properties by solving transient inverse heat conduction problems, Int. J. Therm. Sci. 58 (2012) 113–119.
[10] Y.T. Ren, H. Qi, M.J. He, S.T. Ruan, L.M. Ruan, H.P. Tan, Application of an improved firework algorithm for simultaneous estimation of temperature-dependent thermal and optical properties of molten salt, Int. Commun. Heat Mass Transfer 77 (2016) 33–42.
[11] C.T. Salinas, Inverse radiation analysis in two-dimensional gray media using the discrete ordinates method with a multidimensional scheme, Int. J. Therm. Sci. 49 (2) (2010) 302–310.
[12] M. Dehghani, S.M.H. Sarvari, H. Ajam, Inverse estimation of boundary conditions on radiant enclosures by temperature measurement on a solid object, Int. Commun. Heat Mass Transfer 38 (10) (2011) 1455–1462.
[13] Z.H. Ruan, Y. Yuan, X.X. Zhang, Y. Shuai, H.P. Tan, Determination of optical properties and thickness of optical thin film using stochastic particle swarm optimization, Sol. Energy 127 (2016) 147–158.
[14] A.J.S. Neto, M.N. Özişik, An inverse problem of simultaneous estimation of radiation phase function, albedo and optical thickness, J. Quant. Spectrosc. Radiat. Transf. 53 (4) (1995) 397–409.
[15] T. Ren, M.F. Modest, A. Fateev, A. Clausen, An inverse radiation model for optical determination of temperature and species concentration: development and validation, J. Quant. Spectrosc. Radiat. Transf. 151 (2015) 198–209.
[16] X.C. Wu, Y.C. Wu, J. Yang, Z.H. Wang, B.W. Zhou, G. Grehan, K.F. Cen, Modified convolution method to reconstruct particle hologram with an elliptical Gaussian beam illumination, Opt. Express 21 (10) (2013) 12803–12814.
[17] J.R. Howell, O.A. Ezekoye, J.C. Morales, Inverse design model for radiative heat transfer, ASME J. Heat Transfer 122 (3) (2000) 492–502.
[18] K.J. Daun, F. França, M. Larsen, G. Leduc, J.R. Howell, Comparison of methods for inverse design of radiant enclosures, ASME J. Heat Transfer 128 (2005) 269–282.
[19] N. Bayat, S. Mehraban, S.M.H. Sarvari, Inverse boundary design of a radiant furnace with diffuse-spectral design surface, Int. Commun. Heat Mass Transfer 37 (1) (2010) 103–110.
[20] H.Y. Li, Estimation of thermal properties in combined conduction and radiation, Int. J. Heat Mass Transf. 42 (3) (1999) 565–572.
[21] N. Daouas, A. Fguiri, M.S. Radhouani, Solution of a coupled inverse heat conduction-radiation problem for the study of radiation effects on the transient hot wire measurements, Exp. Thermal Fluid Sci. 32 (8) (2008) 1766–1778.
[22] S.M.H. Sarvari, Inverse determination of heat source distribution in conductive-radiative media with irregular geometry, J. Quant. Spectrosc. Radiat. Transf. 93 (1–3) (2005) 383–395.
[23] K.W. Kim, S.W. Baek, Inverse radiation-conduction design problem in a participating concentric cylindrical medium, Int. J. Heat Mass Transf. 50 (13–14) (2007) 2828–2837.
[24] R. Storn, K. Price, Differential evolution-a simple and efficient heuristic for global optimization over continuous spaces, J. Glob. Optim. 11 (4) (1997) 341–359.
[25] R.P. Chopade, V. Mohan, R. Mayank, R.V.S. Uppaluri, S.C. Mishra, Simultaneous retrieval of parameters in a transient conduction-radiation problem using a differential evolution algorithm, Numer. Heat Transfer A. 63 (5) (2013) 373–395.
[26] H.Y. Li, C.Y. Yang, A genetic algorithm for inverse radiation problems, Int. J. Heat Mass Transf. 40 (7) (1997) 1545–1549.
[27] R. Das, S.C. Mishra, R. Uppaluri, Inverse analysis applied to retrieval of parameters and reconstruction of temperature field in a transient conduction-radiation heat transfer problem involving mixed boundary conditions, Int. Commun. Heat Mass Transfer 37 (1) (2010) 52–57.
[28] R.C. Eberhart, J. Kennedy, Particle swarm optimization, Proceedings of the Sixth International Symposium on Micro Machine and Human Science, 4 1995, pp. 1942–1948.
[29] Y. Yuan, H.L. Yi, Y. Shuai, F.Q. Wang, H.P. Tan, Inverse problem for particle size distributions of atmospheric aerosols using stochastic particle swarm optimization, J. Quant. Spectrosc. Radiat. Transf. 111 (14) (2010) 2106–2114.
[30] H. Qi, L.M. Ruan, H.C. Zhang, Y.M. Wang, H.P. Tan, Inverse radiation analysis of a one-dimensional participating slab by stochastic particle swarm optimizer algorithm, Int. J. Therm. Sci. 46 (7) (2007) 649–661.
[31] A. Colorni, M. Dorigo, V. Maniezzo, Distributed optimization by ant colonies, Proceedings of the First European Conference on Artificial Life, 142 1991, pp. 134–142.
[32] K. Udayraj, P. Mulani, A. Talukdar, R. Das, Alagirusamy, performance analysis and feasibility study of ant colony optimization, particle swarm optimization and cuckoo search algorithms for inverse heat transfer problems, Int. J. Heat Mass Transf. 89 (2015) 359–378.
[33] H. Qi, B. Zhang, Y.T. Ren, L.M. Ruan, H.P. Tan, Retrieval of spherical particle size distribution using ant colony optimization algorithm, Chin. Opt. Lett. 11 (11) (2013) 112901.
[34] A.H. Gandomi, A.H. Alavi, Krill herd: a new bio-inspired optimization algorithm, Commun. Nonlinear Sci. Numer. Simul. 17 (2012) 4831–4854.
[35] S.C. Sun, H. Qi, F.Z. Zhao, L.M. Ruan, B.X. Li, Inverse geometry design of two-dimensional complex radiative enclosures using krill herd optimization algorithm, Appl. Therm. Eng. 98 (5) (2016) 1104–1115.
[36] S. Hajimirza, G.E. Hitti, A. Heltzel, J.R. Howell, Using inverse analysis to find optimum nano-scale radiative surface patterns to enhance solar cell performance, Int. J. Therm. Sci. 62 (2012) 93–102.
[37] R. Das, Forward and inverse solutions of a conductive, convective and radiative cylindrical porous fin, Energy Convers. Manag. 87 (2014) 96–106.
[38] J.C. Bokar, The estimation of spatially varying albedo and optical thickness in a radiating slab using artificial neural networks, Int. Commun. Heat Mass Transfer 26 (3) (1999) 359–367.
[39] H. Qi, C.Y. Niu, S. Gong, Y.T. Ren, L.M. Ruan, Application of the hybrid particle swarm optimization algorithms for simultaneous estimation of multi-parameters in a transient conduction-radiation problem, Int. J. Heat Mass Transf. 83 (2015) 428–440.
[40] E. Cuevas, M. Cienfuegos, D. Zaldívar, M. Pérez-Cisneros, A swarm optimization algorithm inspired in the behavior of the social-spider, Expert Syst. Appl. 40 (16) (2013) 6374–6384.
[41] A. Pasquet, B. Krafft, Cooperation and prey capture efficiency in a social spider, *Anelosimus eximius* (Araneae, Theridiidae), Ethology 90 (2) (1992) 121–133.
[42] K. Ulbrich, J.R. Henschel, Intraspecific competition in a social spider, Ecol. Model. 115 (2–3) (1999) 243–251.
[43] E. Cuevas, M. Cienfuegos, A new algorithm inspired in the behavior of the social-spider for constrained optimization, Expert Syst. Appl. 41 (2) (2014) 412–425.
[44] D.R. Pereira, M.A. Pazoti, L.A.M. Pereira, et al., Social-spider optimization-based support vector machines applied for energy theft detection, Comput. Electr. Eng. 49 (2016) 25–38.
[45] L.A.M. Pereira, D. Rodrigues, P.B. Ribeiro, J.P. Papa, Social-spider optimization-based artificial neural networks training and its applications for Parkinson's disease identification, 2014 IEEE 27th International Symposium on Computer-Based Medical Systems, 2014, pp. 14–17.
[46] S.Z. Mirjalili, S. Saremi, S.M. Mirjalili, Designing evolutionary feedforward neural networks using social spider optimization algorithm, Neural Comput. & Applic. 26 (8) (2015) 1919–1928.
[47] S.C. Mishra, P. Chugh, P. Kumar, K. Mitra, Development and comparison of the DTM, the DOM and the FVM formulations for the short-pulse laser transport through a participating medium, Int. J. Heat Mass Transf. 49 (2006) 1820–1832.
[48] T. Okutucu, Y. Yener, Radiative transfer in participating media with collimated short-pulse Gaussian irradiation, J. Phys. D. Appl. Phys. 39 (2006) 1976–1983.
[49] H.P. Tan, L.M. Ruan, T.W. Tong, Temperature response in absorbing, isotropic scattering medium caused by laser pulse, Int. J. Heat Mass Transf. 43 (2) (2000) 311–320.